TU Delft

Delft University of Technology

Document Version
Final published version

Licence
CC BY

Citation (APA)
Chen, H., Claus, B. B., Song, W., Vildanova, M., van der Poll, L. M., van Aken, A., Vogel, Y. B., Savenije, T. J., Houtepen, A. J., & More Authors (2026). InF3 Surface Passivation on InAs Quantum Dots Enhances Photoluminescence and Reduces Trap-Induced Dark Current in Shortwave Infrared Photodetectors. *ACS Nano*, *20*(34), 23822-23836. https://doi.org/10.1021/acsnano.6c06196

Important note
To cite this publication, please use the final published version (if applicable).
Please check the document version above.

Copyright
In case the licence states “Dutch Copyright Act (Article 25fa)”, this publication was made available Green Open Access via the TU Delft Institutional Repository pursuant to Dutch Copyright Act (Article 25fa, the Taverne amendment). This provision does not affect copyright ownership.
Unless copyright is transferred by contract or statute, it remains with the copyright holder.

Sharing and reuse
Other than for strictly personal use, it is not permitted to download, forward or distribute the text or part of it, without the consent of the author(s) and/or copyright holder(s), unless the work is under an open content license such as Creative Commons.

Takedown policy
Please contact us and provide details if you believe this document breaches copyrights.
We will remove access to the work immediately and investigate your claim.

This work is downloaded from Delft University of Technology.

ACS NANO

www.acsnano.org

Open Access

This article is licensed under CC-BY 4.0

InF_3 Surface Passivation on InAs Quantum Dots Enhances Photoluminescence and Reduces Trap-Induced Dark Current in Shortwave Infrared Photodetectors

Hua Chen, Boris B. Claus, Wenya Song, Marina Vildanova, Lara M. van der Poll, Anne van Aken, Yan B. Vogel, Jing Bai, Yun Hai, Yigithan M. Kose, Maria Isabel Pintor Monroy, Loredana Protesescu, Tom J. Savenije, Zeger Hens, Itai Lieberman, and Arjan J. Houtepen*

Cite This: *ACS Nano* 2026, 20, 23822–23836

Read Online

ACCESS | Metrics & More | Article Recommendations | Supporting Information

ABSTRACT: Shortwave infrared (SWIR) photodetectors are crucial for emerging technologies such as autonomous driving, smart agriculture, industrial inspection, and eye-safe LiDAR. Colloidal indium arsenide (InAs) quantum dots (QDs) offer a low-cost, RoHS-compliant alternative to epitaxial III−V semiconductors. But their performance is limited by a high density of surface trap states that induce nonradiative recombination and potentially give rise to a high dark current in photodiodes. Here, we demonstrate that InF_3 can effectively passivate these surface traps, significantly improving both optical and electronic properties. In nonpolar solvents, a simple InF_3 treatment on oleylamine/chloride-capped In(As,P) and oleate-capped InAs QDs increases the photoluminescence quantum yield to 13% and 4%, respectively—the highest reported for core-only InAs QDs. In polar media, the InF_3 treatment remains effective but reduces colloidal stability. To overcome this limitation, a solid-state *in situ* InF_3 treatment of QD films was used. The treatment doubles the carrier lifetime and lowers the dark carrier density, confirmed by ultrafast transient absorption spectroscopy, microwave conductivity, and electrochemically gated transistor measurements. In SWIR photodetectors, this leads to an order-of-magnitude reduction in dark current density and a 3-fold increase in the calculated specific detectivity, assuming it is shot-noise-limited. Temperature-dependent dark current density and thermal admittance spectroscopy measurements reveal that deep trap states dominate the dark current in InAs QDs photodetectors. The InF_3 treatment strongly suppresses these traps. These findings establish InF_3 passivation as a powerful, promising strategy for mitigating surface-trap-induced dark current and advancing high-performance, RoHS-compliant SWIR photodetectors.

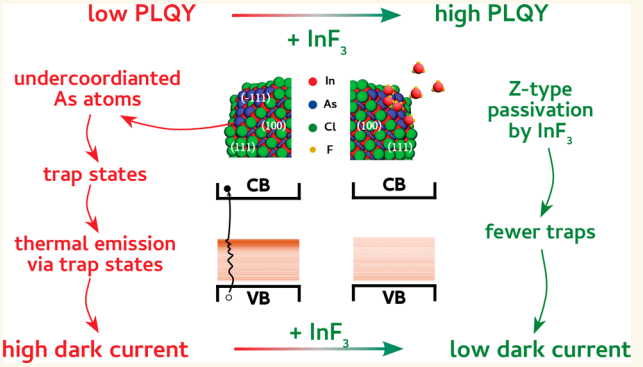

KEYWORDS: *Quantum dots, Indium arsenide, Indium fluoride, Trap states, Surface passivation, Shortwave infrared photodetectors, Thermal admittance spectroscopy*

INTRODUCTION

Shortwave infrared (SWIR) photodetectors enable applications such as autonomous driving, smart agriculture, industrial inspection, biomedical imaging, and light detection and ranging (LiDAR). SWIR light penetrates haze, fog, and tissue more deeply than visible light, enabling high-contrast imaging and 3D sensing.[1−3] However, conventional epitaxial III−V photodetectors remain expensive and difficult to scale. Colloidal quantum dots (QDs) provide a low-cost and scalable alternative due to their solution processability, size-dependent tunability, and complementary metal-oxide-semiconductor (CMOS) compatibility.[4]

Received: April 1, 2026
Revised: July 6, 2026
Accepted: July 28, 2026
Published: August 21, 2026



ACS Publications

© 2026 The Authors. Published by American Chemical Society

Downloaded from pubs.acs.org/ancac3/article-pdf/20/34/23822/6690153/acsnano.6c06196.pdf by TU DELFT user on 22 September 2026

Compared to Hg-based[5] and Pb-based[6] QDs, indium arsenide (InAs) QDs are particularly attractive because they are free of toxic heavy metals and thus compliant with the Restriction of Hazardous Substances (RoHS). The strong infrared absorption and high carrier mobility of bulk InAs make InAs QDs promising candidates for efficient photodetection.[7] e-eto However, InAs QDs suffer from a high density of surface trap states, which are expected to act as nonradiative recombination centers and increase the dark current of photodetectors. Density functional theory (DFT) calculations attribute these trap states primarily to undercoordinated As atoms on the surface, which give rise to deep midgap states.[8−11]

ZnSe shell growth can effectively eliminate surface trap states in InAs QDs.[12] However, such shells impede interdot charge transport, limiting photodetector performance. Extensive efforts have been devoted to mitigating trap-mediated recombination in InAs QDs, including doping,[13] ligand exchange[14−17] and copassivation.[18,19] However, state-of-the-art InAs QD SWIR photodetectors still exhibit dark current densities of 10^{-5}−10^{-6} A cm^{-2}, orders of magnitude higher than those of Pb chalcogenide QDs.[20,21] Most likely, this contrast arises because Pb chalcogenides are surface-tolerant, due to their antibonding valence-band character, which suppresses deep trap formation.[9,22] In contrast, InAs is surface-intolerant, as undercoordinated As 4p orbitals introduce deep electronic states within the band gap.[9,11]

Recently, InF_3 has been shown to effectively passivate surface trap states on InP QDs, enhancing the photoluminescence quantum yield (PLQY) to >90%. It can be introduced either directly[23] or generated *in situ* through etching.[24−26] Possibly, the small size of InF_3 leads to higher surface coverage, thereby eliminating dangling bonds to yield nearly trap-free surfaces. Given the chemical similarity between undercoordinated P on InP and undercoordinated As on InAs,[9] ds it is hypothesized that fluorination should effectively passivate the deep surface traps of InAs QDs, as well. However, this was not experimentally verified. Especially on large InAs QDs absorbing in the SWIR range, the impact of surface passivation on the optoelectronic performance remains unexplored.

In this work, we systematically investigated InF_3 passivation of InAs QDs through multiple approaches and correlated the resulting surface chemistry with optical, electronic, and photodetector performance. First, an InF_3 treatment in nonpolar solvents was applied to In(As,P) QDs capped with oleylamine and chloride and InAs QDs capped with oleate ligands. The treatment increased their PLQYs to 13% and 4%, respectively, the highest values reported for core-only InAs QDs, confirming strongly improved surface passivation. Second, we extended the treatment to QDs dispersed in polar solvents after ligand exchange using $InBr_3$ and ammonium acetate (AA).[15] Although the InF_3 treatment enhances the photoluminescence (PL), the resulting QDs show poor colloidal stability, likely due to their fully fluorinated, weakly charged surfaces. To address this limitation, we implemented an *in situ* InF_3 treatment on $InBr_3$ and AA ligand exchanged InAs QD films. The carrier dynamics were investigated using ultrafast transient absorption (TA) spectroscopy, microwave conductivity and electrochemically gated transistor measurements. The results indicate a doubled carrier lifetime and reduced dark conductivity but also morphological changes that deteriorate the (photo)-conductivity. Finally, when integrated into SWIR photodiodes, the *in situ* InF_3-treated devices exhibit an order-of-magnitude reduction in dark current density and a 3-fold increase in the calculated specific detectivity (assumed to be shot-noise limited) compared to the untreated devices. Beyond demonstrating InF_3 passivation on InAs QDs, we seek to establish a direct correlation between trap-state suppression and dark-current reduction in SWIR photodetectors by investigating the role of trap states in InAs QD photodetectors. Temperature-dependent dark current density−voltage (j−V) measurements reveal that the dark current is thermally activated. Thermal admittance spectroscopy measurements clearly show a large contribution of deep trap states to the dark current of the untreated InAs QD photodetectors, which disappears after the *in situ* InF_3 treatment. Specifically, before the treatment we find a midgap trap states density of 1.7×10^{18} cm^{-3}, which decreases to 3.3×10^{17} cm^{-3}. Collectively, these results establish InF_3 passivation as a promising strategy for mitigating surface-trap-induced dark current in InAs QDs, advancing the development of RoHS-compliant, high-performance SWIR photodetectors.

RESULTS AND DISCUSSION

Trap-Passivated InAs QDs with As-Synthesized Ligands

Recently, we found that InF_3 effectively passivates surface trap states on InP QDs.[23,25] Given the chemical similarity between P and As, we hypothesized that InF_3 could also passivate surface trap states on InAs QDs. As a proof-of-concept, we performed the InF_3 treatment on two types of SWIR absorbing InAs-based QDs: (1) In(As,P) QDs synthesized from aminoarsine precursors and capped with oleylamine ($OlNH_2$) and chloride ligands [In(As,P)-$OlNH_2$/Cl][27] and (2) commercial InAs QDs capped with oleate ligands (InAs-OA). In both cases, the QDs have a tetrahedral shape with average edge lengths of 7.9 ± 0.8 and 9.3 ± 0.8 nm for In(As,P)-$OlNH_2$/Cl and InAs-OA QDs, respectively (Figure S1).

The InF_3 treatment was carried out by adding InF_3 and indium palmitate [$In(PA)_3$] powder into a QD dispersion in hexadecane. The vial was then heated to 180 °C for 60 min. The $In(PA)_3$ added here serves to maintain QD colloidal stability during the treatment, as discussed in our previous work on the InF_3 treatment of InP QDs.[23]

As shown in Figure 1, both as-synthesized QDs have a PLQY of less than 1%, in line with reported values in the literature.[10,28−30] After InF_3 treatment, the PLQYs of In-(As,P)-$OlNH_2$/Cl and InAs-OA QDs increase to 13% (60× increase) and 4% (43× increase), respectively. The increase in PLQY indicates that InF_3 can passivate surface traps on InAs

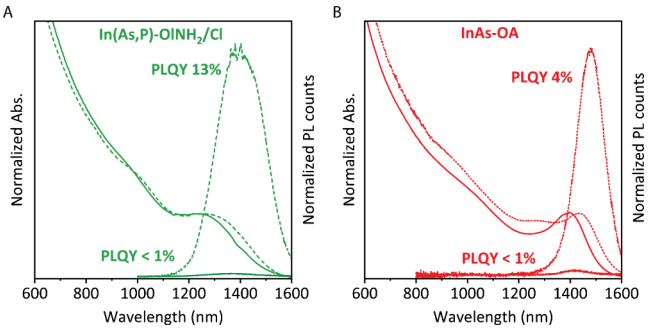

Figure 1. Normalized absorption and PL spectra of (A) In(As,P)-$OlNH_2$/Cl QDs and (B) InAs-OA QDs before (solid lines) and after (dotted lines) InF_3 treatment in hexadecane at 180 °C for 60 min. The PL is normalized by the absorbance of QD dispersions at the excitation wavelength (700 nm).

Downloaded from pubs.acs.org/ancac3/article-pdf/20/34/23822/6690153/acsnano.6c06196.pdf by TU DELFT user on 22 September 2026

https://doi.org/10.1021/acsnano.6c06196
ACS Nano 2026, 20, 23822−23836

QDs regardless of the size and surface ligands. Both the absorption and PL spectra exhibit a red shift after InF_3 treatment (Figure 1). Transmission electron microscopy (TEM) images show no significant change in sizes after the treatment (Figure S1). We ascribe the observed red shift to the change in the electronic structure upon fluorination.[31] After InF_3 treatment, a peak around 685 eV was observed in X-ray photoelectron spectroscopy (XPS) F 1s spectrum of both samples, which corresponds to InF_3,[24] demonstrating the presence of InF_3 (Figure S2 and Table S1). However, considering the limited solubility of InF_3 in nonpolar solvents, it remains unclear how InF_3 dissolves in hexadecane and accesses the QD surface.

The PLQYs obtained after InF_3 treatment are record-high values for InAs core-only QDs.[7,10,28−30,32] However, a PLQY of 13% remains well below the near-unity PLQY obtained for InP QDs using a similar surface treatment.[23] This suggests that additional nonradiative pathways remain after fluorination, highlighting a fundamental difference between those of InP and InAs. There is possibly an inherent challenge to attain high PLQY in the SWIR range, where electric-dipole, near-field energy transfer between the QD electronic transitions and the infrared vibrational modes of ligands or solvent can enhance nonradiative energy loss.[33] Still, the PLQYs of InAs/ZnSe core/shell QDs[12] and Pb chalcogenide QDs[34,35] emitting at comparable wavelengths are considerably higher. Alternatively, full-surface passivation may be more difficult to achieve on InAs than on InP.

InF_3-Treated Photoconductive InAs QD Films

QD-based photodetectors require an efficient charge transport across the QD film. Therefore, the long-chain insulating ligands present on as-synthesized QDs must be replaced with shorter, more conductive ones.[36] In the InF_3 treatment described above, insulating $In(PA)_3$ ligands are present on the surface to maintain colloidal stability in the nonpolar solvent. Therefore, we explored the possibility of making an InAs QD ink with InF_3 surfaces via a phase-exchange reaction. The full width at half-maxima (fwhm) of the PL peaks of the as-synthesized $In(As,P)$-$OINH_2$/Cl and as-received InAs-OA QDs are 168 and 82 meV, respectively (Figure 1). The narrower emission line width indicates that InAs-OA QDs are more homogeneous in both size (Figure S1) and possibly composition, resulting in a more ordered energy landscape that is favorable for charge transport in devices. Therefore, we selected InAs-OA QDs for all of the subsequent studies.

However, attempts to transfer InAs QDs from nonpolar to polar solvents by only adding InF_3 invariably resulted in the complete precipitation of the QDs. Next, we tested a two-step approach. The QDs were first treated with InF_3 in nonpolar solvents. Then, they were transferred to polar solvents using the $InBr_3$ and ammonium acetate (AA) ligand exchange protocol.[15] The ligand-exchange procedure worked well for InF_3-treated InAs-OA QDs, allowing stable dispersion in *N*,*N*-dimethylformamide (DMF). However, we observed a significant PL decrease after $InBr_3$/AA ligand exchange, which suggests that the added InF_3 moieties are largely removed during phase transfer. Therefore, we next explored the possibility of performing the InF_3 treatment after $InBr_3$/AA ligand exchange.

As shown in Figure 2A, the PL intensity of InAs QDs ligand-exchanged with $InBr_3$ and AA (InAs-$InBr_3$/AA, green curves) decreased compared to the QDs with native ligands (InAs-OA, blue curves). This is a common outcome of aggressive ligand exchange processes.[37,38] Subsequent InF_3 treatment of the

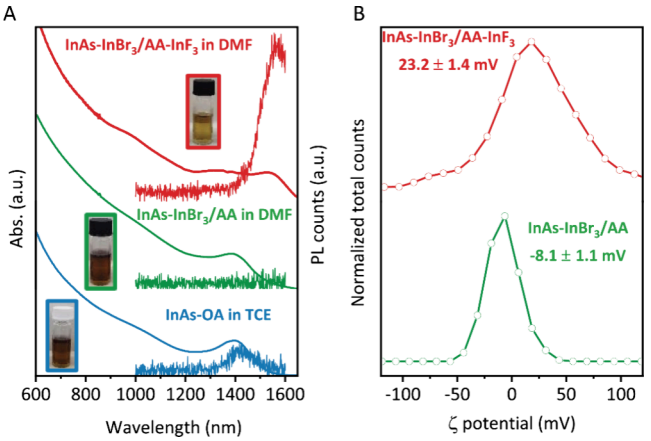

Figure 2. (A) Absorption and PL spectra of InAs QDs with native ligands (InAs-OA, blue curves), InAs QDs ligand exchanged with $InBr_3$ and AA (InAs-$InBr_3$/AA, green curves), and ligand-exchanged InAs QDs treated with InF_3 (InAs-$InBr_3$/AA-InF_3, red curves). Insets are photographs of QD dispersions after filtration through 0.2 μm PTFE syringe filters. (B) ζ potentials of ligand-exchanged QDs before (green curve) and after (red curve) InF_3 treatment.

ligand-exchanged QDs strongly enhanced the PLQY by a factor 46 to 4.3%, which is similar to the effect we observed in nonpolar solvents (Figure 1B). This confirms the improved passivation of surface traps by InF_3 in polar solvents. The absorption and PL peaks redshift after treatment, similar to observations in nonpolar solvents. However, the InF_3-treated QDs again exhibit poor colloidal stability, and only 15% of the QDs were retained in the ligand-exchanged sample (Figure S3), as is clear from the lighter color of the resulting dispersion in Figure 2A.

In polar solvents, colloidal stability is maintained by electrical double layer formed by sufficient surface charge and counter-ions. We hypothesize that the net surface charge is decreased after InF_3 treatment. To test our hypothesis, we performed ζ-potential measurements on the filtered QD dispersions. The results, shown in Figure 2B, are unexpected. The $InBr_3$/AA ligand-exchanged QDs have a ζ potential of around −8 mV, which is nearly neutral and consistent with literature.[15] Despite this low ζ potential, the QDs remain colloidally stable in DMF. It is likely that the presence of acetate is responsible for the small net negative surface charges. Indeed, Protesescu et al. have shown that, on InP QDs, ligand exchange using metal halides in DMF without AA gives rise to a positive ζ potential, indicating a net positively charged surface.[39] After InF_3 treatment, the ζ potential becomes positive and shows a broader distribution, indicating significant changes in surface chemistry. We speculate that acetate might be removed from the surface, making the surface positively charged again. However, it remains unclear what exactly causes the loss of colloidal stability.

The results on the colloidal ligand exchange and trap passivation strategy demonstrate that InF_3 effectively passivates surface traps of ligand-exchanged InAs QDs in polar solvents. However, the considerable loss of QDs during the treatment renders this approach impractical to prepare QD inks for device fabrication.

Given the lack of colloidal stability after solution-phase InF_3 treatment, we explored a solid-state approach by applying InF_3 passivation to $InBr_3$/AA ligand-exchanged InAs QD films. We first treated the films by submerging them in hexadecane, adding solid InF_3 directly and heating to 150 °C. While this enhanced the PL, the improvement was modest, possibly due to the low

Downloaded from pubs.acs.org/ancac3/article-pdf/20/34/23822/6690153/acsnano.6c06196.pdf by TU DELFT user on 22 September 2026

https://doi.org/10.1021/acsnano.6c06196
ACS Nano 2026, 20, 23822−23836

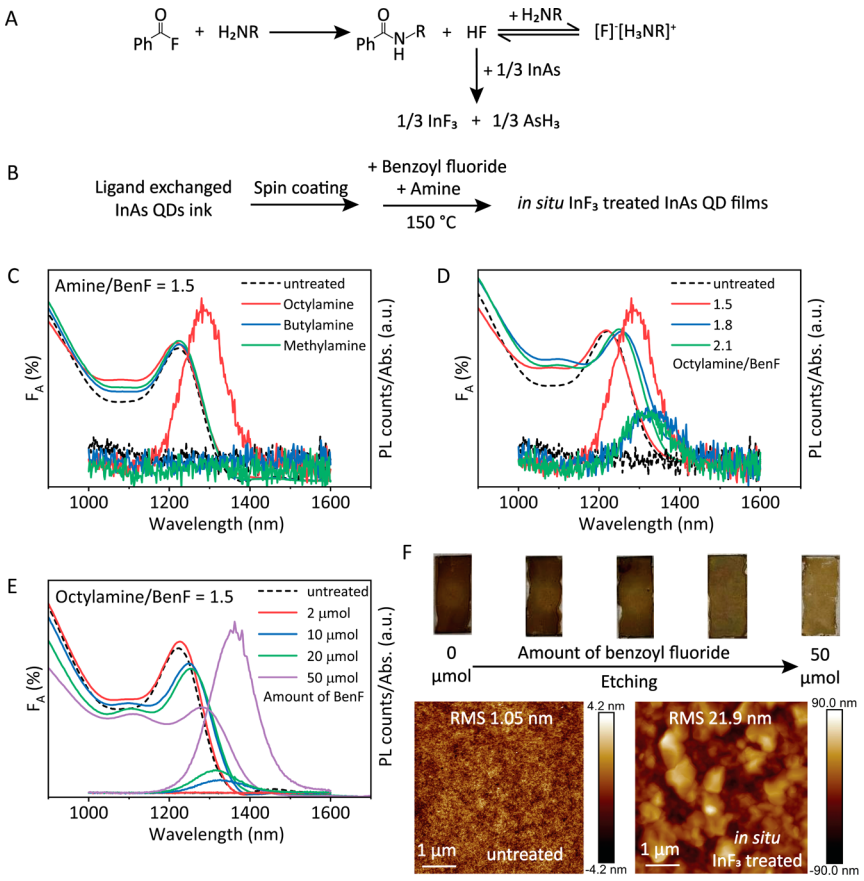

Figure 3. (A) Scheme of the reaction between BenF, amine, and InAs with an amine:BenF ratio of 1.5:1. (B) Illustration of solid-state *in situ* InF_3 treatment on ligand-exchanged InAs QD films. Absorption and PL spectra of InAs QD films treated with different (C) amines, (D) amine to BenF ratios, and (E) amount of BenF. (F) Morphology of *in situ* InF_3-treated InAs QD films. (Top) Photographs of samples in part E. (Bottom) AFM images of untreated and *in situ* InF_3-treated QD films.

solubility of InF_3 in hexadecane. Therefore, we attempted generating InF_3 *in situ*, similar to the approach we followed previously for InP QDs.[25] In this approach, benzoyl fluoride (BenF) and a primary amine undergo an amidation reaction to produce hydrogen fluoride (HF) *in situ*; see the reaction mechanism in Figure 3A. The generated HF partially etched the InAs QDs via InAs + 3HF → InF_3(s) + AsH_3(g). The produced InF_3 remains, in part on the QD surface, passivating As surface atoms, while the arsine gas escapes. This results in a net loss of InAs material via etching, the extent of which can be controlled by the reaction conditions (*vide infra*). The etching can however not be fully avoided, as it is required to produce InF_3 *in situ*.

As shown schematically in Figure 3B, the passivation procedure involved placing spin-coated InAs QD films into hexadecane and heating the solution to 150 °C, followed by sequential addition of amine and BenF. The films were maintained under these conditions for 15 min. To optimize the treatment, we systematically investigated the effects of amine chain length, the molar ratio between amine and BenF, and the total precursor amount on PL performance. We initially varied the amine chain length with the aim of identifying short ligands that could function as L-type donors at anionic surface sites without promoting QD dissolution into the nonpolar medium. As shown in Figure 3C, amidation with octylamine results in strong PL enhancement, while shorter amines, such as butylamine and methylamine, are ineffective. We speculate that the solubility of the benzamide product that forms in the amidation reaction is lower for the shorter amines, which makes the reaction less thermodynamically favorable.

Next, we explored the effect of the amine/BenF ratio. Additional amine removes HF in the acid–base equilibrium shown in Figure 3A and therefore modulates the degree of etching.[25,26] As shown in Figure 3D, a 1.5:1 ratio yielded the most significant PL increase, while higher ratios gave only moderate PL enhancement. This is because excess amine consumes HF, limiting InF_3 formation and thus surface passivation.

To further evaluate the extent of passivation and etching, we varied the total amount of BenF added while maintaining the 1:1.5 ratio with octylamine. As shown in Figure 3E, increasing the precursor concentration further enhanced the PL, demonstrating that more InF_3 is present on the surface. However, this also leads to increased QD etching, as evidenced by the reduced 1S absorption feature (Figure 3E) and a noticeable thinning of the film (Figure 3F, top). Atomic force microscopy (AFM; Figure 3F, bottom) confirmed that the treated films exhibited increased surface roughness, likely due to material loss during the HF-mediated etching process.

Together, these results confirm that solid-state *in situ* InF_3 passivation significantly improves the optical properties of InAs QD films, but the trade-off is a degree of irreversible film damage due to etching. Since the etching is required to form InF_3 for surface passivation, it cannot be fully eliminated. Nevertheless, this approach provides a controllable route to achieving effective surface trap state passivation in the solid state, avoiding the

https://doi.org/10.1021/acsnano.6c06196
ACS Nano 2026, 20, 23822−23836

Downloaded from pubs.acs.org/ancac3/article-pdf/20/34/23822/6690153/acsnano.6c06196.pdf by TU DELFT user on 22 September 2026

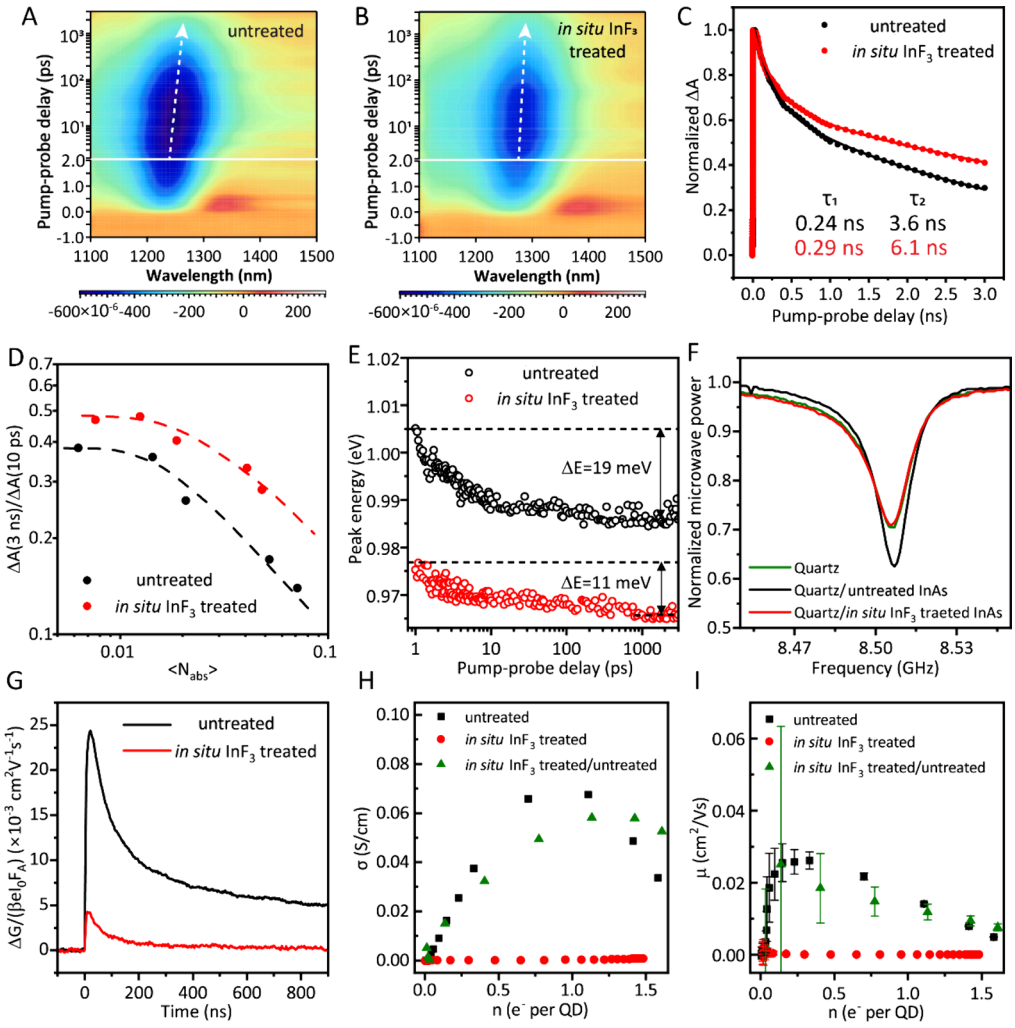

Figure 4. Carrier dynamics of InAs QD films before and after *in situ* InF_3 treatment. 2D TA heat maps of untreated (A) and treated (B) films. The white dashed arrows indicate the evolution of the 1S bleach peak. (C) Normalized bleach decay traces (dots) with biexponential fits (solid lines). (D) Excitation intensity dependence of the bleach amplitude ratio at 3 ns and 10 ps and (E) time-dependent 1S bleach peak energy showing spectral diffusion in untreated (black circles) and treated (red circles) films. (F) DMC frequency scans and (G) TRMC measurements for photoexcitation at 700 nm with 1.5×10^{13} photons cm^{-2} per pulse. Charge-carrier-density-dependent (H) conductivities and (I) mobilities of untreated film (black squares), *in situ* InF_3-treated film (red circles), and two-layer sample prepared by spin coating another untreated film on the treated one (green triangles). The error bar of measured mobilities is determined by the optical detection limit of our setup, which is ±1 mOD.

colloidal instability observed in polar solvents. Future improvements should focus on how to minimize etching to avoid material loss and maintain the morphology. Instead of *in situ* HF formation, the addition of indium and fluoride salts to form InF_3 directly inside the film is a promising direction. Furthermore, solution-processable inks are preferred for device fabrication. This would require engineering the surface composition to retain sufficient surface charge after fluorination, thereby maintaining the colloidal stability.

Carrier Dynamics of Trap-Passivated InAs QD Films

The *in situ* InF_3 treatment proved to be a successful strategy for enhancing the PLQY of conductive QD films. To investigate the effect of InF_3 passivation on the optoelectronic properties of InAs QD films, we used femtosecond TA spectroscopy, microwave conductivity, and electrochemically gated transistor measurements. Parts A and B of Figure 4 show 2D TA images, which present the absorption change as a function of time and probe wavelength. Both films exhibit a clear 1S absorption bleach after photoexcitation at 700 nm. The decay traces reveal that InF_3 passivation increases the photocarrier lifetime (Figure 4C): the intensity-averaged lifetime calculated from biexponential fits to the 1S bleach decay (solid lines in Figure 4C) increases from 3.5 to 6.0 ns, in line with the observed improvement in PLQY upon passivation (Figure 3).

In addition, excitation-intensity-dependent TA measurements (Figure S5) demonstrate slower recombination at lower excitation densities. We plot the ratio of the absorption bleach at 3 ns vs the bleach at 10 ps, i.e., $\Delta A(3\text{ ns})/\Delta A(10\text{ ps})$, in Figure 4D. This ratio decreases as the pump fluence increases, indicating that the fraction of decaying carriers increases with the excitation density. This behavior is a well-known signature of Auger recombination. Importantly, even at an average exciton occupancy as low as $< N_{abs} > \approx 0.01$ absorbed photons per QD, a residual fast-decay component is still evident. This is similar to previous observations in conductive PbSe QD solids, where ultrafast charge carrier diffusion leads to efficient Auger recombination even at extremely low excitation densities.[40] We ascribe the persistent fast decay in our films to similar

Downloaded from pubs.acs.org/ancac3/article-pdf/20/34/23822/6699153/acsnano.6c06196.pdf by TU DELFT user on 22 September 2026

https://doi.org/10.1021/acsnano.6c06196
ACS Nano 2026, 20, 23822−23836

diffusion-mediated Auger processes: the high mobility of carriers within the QD films allows charge carriers to migrate and congregate in larger QDs due to energy disorder, where they undergo Auger recombination.

Fast charge carrier diffusion in combination with energy disorder also results in spectral diffusion.[41] Indeed, both untreated and *in situ* InF_3-treated InAs QD films exhibit a time-dependent redshift of the TA bleach peak, as indicated by the white arrows in Figure 4A,B. Figure 4E shows the 1S bleach maximum as a function of time for treated and untreated films. After InF_3 treatment, the observed spectral diffusion is smaller than that of the untreated film. If the carrier mobilities are the same, the sample with higher energy disorder is expected to show larger red-shift.[42] The energy disorder can be quantified by the fwhm of the 1S absorption peak, which increases from 88 to 103 meV after the treatment. Given that the treated sample exhibits less spectral diffusion while the energy disorder is larger, we conclude that the carrier mobility likely decreases, potentially because increased QD polydispersity hampers the dot-to-dot charge transport within the film.

To further quantify the conductivity of the films, we employed dark microwave conductivity (DMC) and time-resolved microwave conductivity (TRMC) measurements.[43,44] DMC measures the dark conductivity by monitoring the change in reflected microwave power in a cavity at resonance due to free carrier absorption, providing insight into the background charge carrier density. A sample with higher (dark) conductivity will absorb more microwave power and result in a lower signal at the cavity resonance frequency of around 8.51 GHz. As shown in Figure 4F, InF_3-treated films exhibit significantly reduced dark conductance, approaching the detection limit of the system (equal to the blank DMC measurement on quartz). By fitting the DMC frequency scan, we can quantify the dark conductivity (σ_{dark}) (see the Experimental Section for more details).[44] In the untreated InAs QD film, σ_{dark} is determined to be 0.026 S cm^{-1}. After the *in situ* InF_3 treatment, due to the limit in the sensitivity of the measurement, the upper limit of σ_{dark} is 0.002 S cm^{-1}. This reduction in σ_{dark} can be ascribed to the decrease in the dark carrier density. We will come back to this point below.

TRMC was then used to assess photoconductivity. The photoconductance (ΔG) signals are normalized by a geometric factor (β), the elementary charge (e), the laser intensity (I_0), and the fraction of photons that are absorbed at the excitation wavelength (F_A). This yield the product $\Phi_{max}\sum\mu$, representing the yield of free electrons and holes (Φ_{max}) and the sum of their mobilities ($\sum\mu$).[44,45] For QD samples with high dielectric constants, and consequently relatively small exciton binding energies, the yield of free charge generation is usually close to 1 at room temperature[45,46] such that changes in $\Phi_{max}\sum\mu$ reflect changes in the electron and hole mobility. For both samples, $\Phi_{max}\sum\mu$ decreases with increasing excitation intensity due to higher-order recombination within the 18 ns instrument response time, set by the microwave cavity that is used (Figure S6). Figure 4G shows TRMC transients at an excitation intensity of 1.5×10^{13} photons cm^{-2} per pulse, which is close to the linear regime (Figure S6). For the untreated InAs QD film, $\Phi_{max}\sum\mu$ is ~0.0243 $cm^2\ V^{-1}\ s^{-1}$, and the photoconductivity decays to half of the maximum value in 144 ns. For the treated film, $\Phi_{max}\sum\mu$ is reduced to ~0.0042 $cm^2\ V^{-1}\ s^{-1}$ while the half-life time of the photoconductance decreases to 64 ns.

Combining DMC and TRMC measurements, the carrier density in the dark (n_{dark}) can be calculated from the dark conductivity (σ_{dark}) and the sum of mobilities ($\sum\mu$) via $n_{dark}=e\sum u/\sigma_{dark}$. As shown in Table S2, n_{dark} decreases from 6.7×10^{18} cm^{-3} to less than 3.4×10^{18} cm^{-3} after *in situ* InF_3 treatment. n_{dark} in the treated film should explicitly be seen as an upper limit since the dark conductivity of this sample is not higher than that of the quartz substrate. Nevertheless, we can conclude that there is a clear reduction in dark carrier density, in line with increased PLQY and carrier lifetime seen in TA experiments (Figure 4C), confirming the passivation of surface trap states by InF_3.

Given the 3−6 ns lifetime measured with TA (Figure 4C) and the 18 ns instrument response time of the resonance cavity used in TRMC measurements, we estimate that only ~5% of the photogenerated carriers are detected. Hence the measured values of $\Phi_{max}\sum\mu$ present a lower limit to carrier mobility. Even so, these results suggest that the mobility decreases after the *in situ* InF_3 treatment, in line with the reduced spectral diffusion shown in Figure 4E. This could be due to the use of octylamine in the treatment, which can bind to the QD surface as L-type ligand and thereby increase the QD interdistance.[26] However, the reduced mobility could also result from a reduction in film quality, leading to cracks that impede transport.

The sensitivity of the mobility to such cracks depends on the technique used to measure the charge transport.[47] TA probes transport via spectral diffusion in $\tau \approx 10$ ps, while TRMC probes carrier diffusion during half a period of the 8.5 GHz microwave field, i.e., in $\tau \approx 60$ ps. With a mobility of 10^{-2} $cm^2\ V^{-1}\ s^{-1}$ this would mean TA probes a length scale of $L = \sqrt{\frac{\mu\tau}{kT}} \approx 50$ nm, while TRMC probes ~120 nm. Changes in film morphology on this length scale will thus influence the measured mobility. In contrast, transistor measurements probe DC charge transport over a length scale that is set by the distance between the source and the drain electrodes, typically 10−50 μm. The relevant length scale for transport in photodiodes is the thickness of the photoactive film, typically 200−300 nm.[2,15,18−20] Thus, this is intermediate between TRMC and transistor measurements.

To investigate the long-range DC transport, we used electrochemically gated transistor measurements.[48−52] A gate voltage is applied between a QD film and a reference electrode in a liquid electrolyte to modulate the charge carrier density which is accurately determined by *in situ* monitoring the absorption bleach at the 1S peak due to state filling via $n_{1S} = 2\Delta A/A_0$.[51,52] Here, the factor 2 reflects the degeneracy of the $1S_e$ level in InAs QDs.[51] To obtain the conductivity and mobility of the QD film at various potentials, a linear bias sweep is applied between source and drain electrodes with a gap size of 25 μm at each gate voltage, see Figure S7. The charge-carrier-density-dependent conductivity and mobility are plotted in Figure 4H,I. As shown in Figure 4H, the conductivity of the untreated InAs QD film (black squares) first increases with n_{1S} and reaches a maximum of 0.064 S cm^{-1} when around 1 electron per QD ($n_{1S} = 1$) is electrochemically injected into $1S_e$ level. When more electrons are injected, the conductivity drops. This is expected because the $1S_e$ levels become completely filled and electron transport through this level is impeded.[47,53] The low effective mass in InAs causes the $1P_e$ levels to be separated from the $1S_e$ levels by more than 150 meV,[54] so that conduction through the $1P_e$ levels is not significant.

However, after *in situ* InF_3 treatment, the conductivity drops significantly (red circles in Figure 4H). This reduction may arise from two factors: (1) impaired interparticle charge transport due to altered surface chemistry or (2) morphological disruptions such as cracks that hinder long-range transport across the 25 μm

Downloaded from pubs.acs.org/ancac3/article-pdf/20/34/23822/6699153/acsnano.6c06196.pdf by TU DELFT user on 22 September 2026

https://doi.org/10.1021/acsnano.6c06196
ACS Nano 2026, 20, 23822−23836

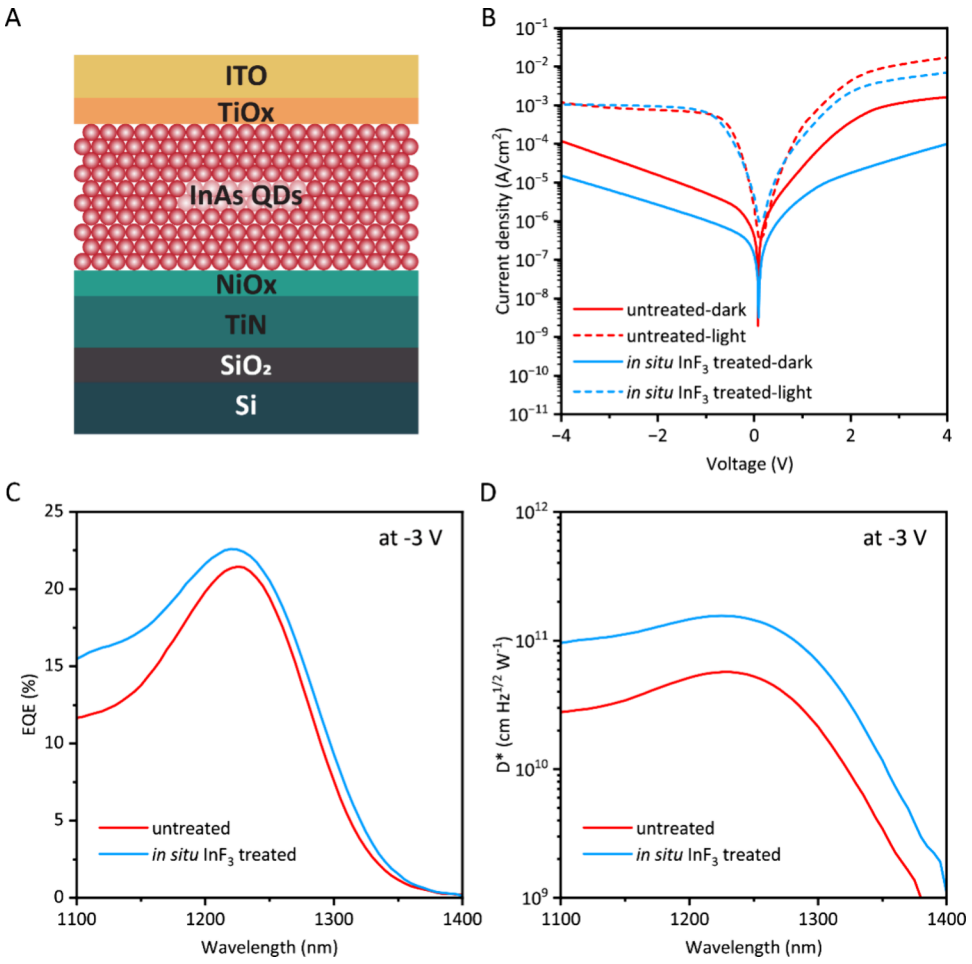

Figure 5. Performance of SWIR photodetectors fabricated using untreated and *in situ* InF_3-treated InAs QD films. (A) Schematic device structure. (B) *j*−*V* characteristics under dark (solid lines) and under IR illumination (dashed lines). (C) EQE and (D) specific detectivity of devices biased at −3 V calculated assuming shot-noise-limited.

electrode spacing. To distinguish between these effects, an additional layer of ligand-exchanged InAs QDs (identical to the as-deposited film) was spin coated on top of the treated film. As shown in Figure 4H, the conductivity of the bilayer structure (green triangles) is restored to a level comparable to the untreated film. This recovery suggests that dot-to-dot charge transport remains efficient and that the dominant limitation to macroscopic conductivity arises from film discontinuities introduced during the *in situ* InF_3 treatment, consistent with the AFM images shown in Figure 3F.

The carrier-density-dependent mobilities of all three samples are plotted in Figure 4I. In the untreated film, the mobility increases sharply at low charge carrier density region and reaches a maximum of 0.026 $cm^2\ V^{-1}\ s^{-1}$. This activation behavior is ascribed to energy disorder in the QD film.[47] Although mobility strongly depends on the charge carrier density, the mobility obtained from electrochemically gated transistor measurements is similar to that from TRMC measurements. After the *in situ* InF_3 treatment, the low mobility indicates very poor transport over the 25 μm source−drain distance, caused by morphological changes such as macroscopic cracks.

To summarize the optoelectronic characterization, the *in situ* InF_3 treatment effectively passivates surface trap states in InAs QD films, as evidenced by prolonged carrier lifetimes, reduced dark conductance, and enhanced PLQY. However, in addition to these improvements, a decrease in the film conductivity is observed due to morphological changes in the film. Electrochemically gated transistor measurements confirm that the primary limitation arises from macroscopic film discontinuities rather than impaired dot-to-dot transport. These findings indicate that the InF_3 treatment as introduced here involves a trade-off between trap passivation and transport efficiency.

Trap-Passivated InAs QDs Photodetector Performance

To evaluate the effect of InF_3 passivation on the photodiode performance, we fabricated SWIR photodetectors using a spin-coated InAs QD layer with and without *in situ* InF_3 treatment. For photodetectors, we found a bilayer structure as in the electrochemically gated transistor measurements was not needed, because charge transport takes place in the ∼200 nm thickness direction of the film. The devices consist of a multilayer stack of TiN/NiO_x/InAs QDs/TiO_x/ITO on a Si substrate (Figure 5A). The concentrations of BenF and octylamine used in *in situ* InF_3 treatment were optimized to achieve effective surface passivation while minimizing etching. The scanning electron microscopy (SEM) cross section of the devices before and after *in situ* InF_3 treatment are shown in Figure S8. There is no significant decrease in the thickness of the QD layer after treatment. However, we do observe a slight increase in roughness at the interface between InAs QD and TiOx, which we ascribe to the etching during the treatment, in line with the AFM images shown in Figure 3F. Figure 5B shows

https://doi.org/10.1021/acsnano.6c06196
ACS Nano 2026, 20, 23822−23836

Downloaded from pubs.acs.org/ancac3/article-pdf/20/34/23822/6699153/acsnano.6c06196.pdf by TU DELFT user on 22 September 2026

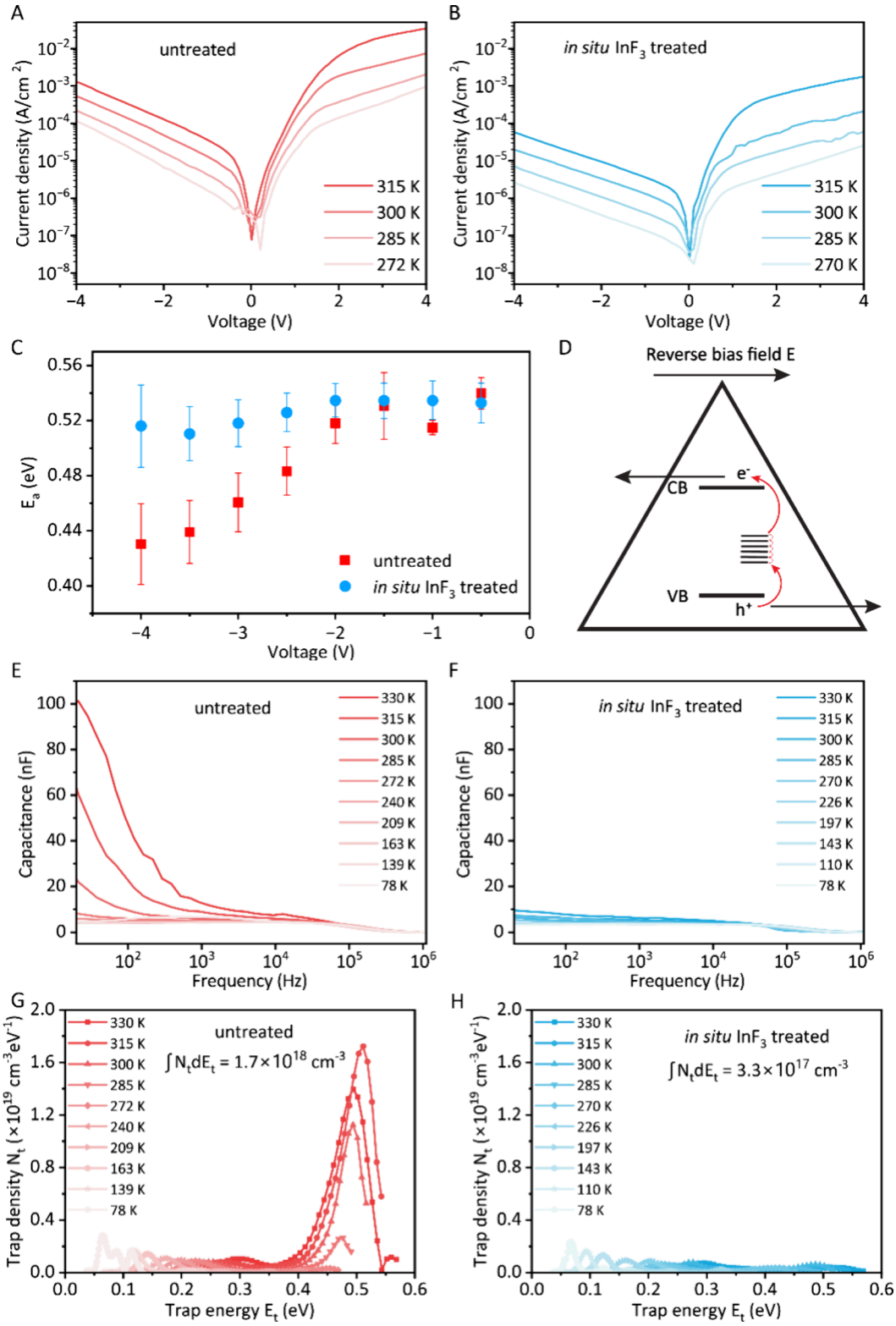

Figure 6. Temperature-dependent *j*−*V* and *C*−*f* characteristics. Dark current densities measured in the range of 270−315 K of (A) untreated and (B) *in situ* InF_3-treated devices. (C) Activation energy extracted from Arrhenius plots at various reverse biases. (D) Scheme of thermal emission of carriers via midgap states. The *C*−*f* plots measured in the range of 78−330 K and the reconstructed trap density distributions of (E and G) untreated and (F and H) *in situ* InF_3-treated devices.

j−*V* curves of untreated and InF_3-treated photodiodes, both in the dark and under 1200 nm LED illumination with a power density of ∼3.5 mW cm^{-2}. Most notably, the dark current density decreases by an order of magnitude after the *in situ* InF_3 treatment, while the photocurrent increases marginally. As a result, the treated device exhibits a photocurrent to dark current ratio of 115 at a reverse bias of −3 V and the given illumination power, which is significantly higher than the ratio of 27 for the

Downloaded from pubs.acs.org/ancac3/article-pdf/20/34/23822/6990153/acsnano.6c06196.pdf by TU DELFT user on 22 September 2026

https://doi.org/10.1021/acsnano.6c06196
ACS Nano 2026, 20, 23822−23836

untreated device. We assign this to a reduction in surface trap states, consistent with the higher PLQY and the prolonged carrier lifetime. Moreover, the dark $j-V$ characteristics of six individual devices from one substrate are shown in Figure S9. The small distribution of dark current densities indicates good uniformity.

Figure 5C presents the wavelength-dependent external quantum efficiency (EQE) measured at −3 V. After the *in situ* InF_3 treatment, the peak EQE is 23%, vs 22% for the untreated sample. We calculated the specific detectivity assuming it is shot-noise-limited (D^*_{shot}). The maximum D^*_{shot} of the *in situ* InF_3-treated device reaches a value of 1.55×10^{11} cm $Hz^{1/2}$ W^{-1} at 1220 nm, 3 times larger than that of the untreated device (Figure 5D).

Mechanistic Insight into the Correlation between Trap States and Dark Current

While it is well established that trap states in semiconductor materials act as nonradiative recombination centers and are generally expected to elevate dark current,[55−59] the quantitative correlation between trap state density and dark current in InAs QD-based SWIR photodetectors remains poorly understood.

To gain deeper insight into the role and nature of trap states in the dark current of InAs QD-based SWIR photodetectors, we performed temperature-dependent dark $j-V$ measurements in the range of 270−315 K. As plotted in Figure 6A, heating the untreated device to 315 K increases the dark current density to 430 μA cm^{-2} at −3 V while cooling to 272 K decreases it to 30 μA cm^{-2}. Similarly, the dark current density of the *in situ* InF_3-treated device drops from 23 μA cm^{-2} at 315 K to 1 μA cm^{-2} at 270 K (Figure 6B). Clearly, the dark current is thermally activated in both devices. We extracted activation energies (E_a) at various reverse bias values from Arrhenius plots (Figure S10). In the untreated device, E_a is 0.53 eV at −0.5 V and decreases to 0.43 eV at −4 V (Figure 6C). The reduction in E_a with increasing reverse bias is characteristic of field-assisted emission from trap states, consistent with a trap-mediated dark current under high electric field.[20,60] After *in situ* InF_3 treatment, the device shows similar E_a at small reverse bias, but E_a only decreases to 0.51 eV at −4 V. The weakly reverse-bias-dependent E_a suggests the suppression of trap-mediated pathways. The optical band gap (E_g) of InAs QDs used in these devices is 1.02 eV. The E_a extracted at low reverse bias is around $E_g/2$. Therefore, we ascribe this thermally activated process to the emission of carriers via midgap trap states, as illustrated in Figure 6D. We note that thermal generation of charge carriers via trap states would be limited by the largest energy gap in the distribution of traps states in the band gap. This gap is about half of the band gap, but it is conceivable that there is a distribution of trap states from the valence band top to midgap, as is predicted by DFT calculations on InAs QDs with exposed As terminated (−1−1−1) facets.[9,11]

To identify the dominant trap state in InAs QDs and quantify how effectively the *in situ* InF_3 treatment passivates them, we performed thermal admittance spectroscopy (TAS) measurements in the range of 78−330 K at 0 V. The capacitance-frequency ($C-f$) spectra were extracted by assuming a parallel RC circuit. We note that a proper equivalent circuit of these devices with multiple layers and disordered transport in the QD layer is most likely very complex. Therefore, we checked that similar results are obtained for a series RC circuit, demonstrating that the exact equivalent circuit used is not critical for the ensuing analysis of the trap state distribution.

The basis of TAS is that an AC bias increases or decreases the depletion width in the photodiode. Increasing the depletion width involves both extracting mobile majority carriers from the 1S levels of the InAs QDs, and carriers from trap levels inside the band gap. At high frequencies, the capacitance is due to the majority carriers in the junction. The associated drop in capacitance is often referred to as the dielectric relaxation step. It depends strongly on the carrier mobility and is usually observed at frequencies of $>10^4$ Hz. Since trap emission is much slower than mobile majority carrier transport, only traps with an emission rate that is larger than the angular frequency (ω) of the AC bias contribute to the capacitance, resulting in a characteristic drop in the capacitance-frequency spectra at low frequencies (typically 10^0-10^4 Hz).[61]

The trap emission rate (e_t) depends on the temperature as $e_t = \nu_0 e^{(-E_t/k_B T)}$, where ν_0 is an effective attempt-to-escape frequency and E_t is the trap energy away from the band edges. Therefore, at each temperature, the measurement probes a different energy window of traps, and the characteristic trap frequency in the $C-f$ spectra increases with increasing temperature. Combining frequency and temperature dependence of the trap-related capacitance these two parts, the trap density distribution $[N_t(E_t)]$ can be reconstructed.[61,62] A more detailed description can be found in Supplementary Note 1.

As shown in Figure 6E, the untreated device exhibits a large capacitance at low frequencies ($<10^3$ Hz), and the capacitance increases with temperatures. This is clear evidence of deep trap states. After *in situ* InF_3 treatment, the capacitance measured at all temperatures is lower, indicating suppression of traps over a large energy range. The capacitance measured at low frequencies is significantly decreased, demonstrating that deep traps are especially removed (Figure 6F). As plotted in Figure S11, we extracted the characteristic trap frequency (also known as the demarcation energy) from the minimum of the ω $dC/d\omega$ vs ω plots at different temperatures. From an Arrhenius plot of this trap frequency for the untreated ν_0 is determined to be 1.5×10^{10} s^{-1}. This is within the range of 10^8-10^{10} s^{-1} reported in literature for PbS QDs[63−65] and small organic semiconductors.[66] ν_0 measured in InAs QDs in this work is lower than that reported for bulk crystalline semiconductors[62] ($\sim 10^{12}$ s^{-1}) possibly because interaction between various traps in the band gap.[61] The activation energy of the trap emission is determined to be 0.55 eV, which aligns with the dark current activation energy at small reverse bias (Figure 6C). This suggests that the thermally activated processes observed from TAS and dark current measurements relate to the same, deep trap states near the middle of the gap.

In TAS, the trap density can be determined via $N_t(E_t) = \frac{V_{bi}}{eW}\frac{\omega}{k_B T}\frac{dC}{d\omega}$.[62] Here V_{bi} is the built-in potential, and W is the depletion width of the junction. To determine these values, we applied Mott−Schottky analysis on the capacitance−voltage ($C-V$) measurements at 300 K, as explained in the Supporting Note 1. As shown in Figure S12 and Table S3, the extracted V_{bi} and W are 1.1 V and 85 nm for both samples. While these extracted parameters should be treated with caution, and seen as a rough estimate, we note that a possible error in these values would partially cancel out in the determination of $N_t(E_t)$. Further, we note that these values only change the absolute value of the trap distribution, not the energy dependence. The reconstructed trap density distribution for the untreated and the *in situ* InF_3-treated devices are shown in Figure 6G,H, respectively. In the untreated device, a pronounced Gaussian-

Downloaded from pubs.acs.org/ancac3/article-pdf/20/34/23822/6990153/acsnano.6c06196.pdf by TU DELFT user on 22 September 2026

https://doi.org/10.1021/acsnano.6c06196
ACS Nano 2026, 20, 23822−23836

like distribution of deep trap states located at 0.5 eV and a tail of shallow traps ranging toward the band edge are observed. From these measurements alone we cannot tell whether this band of traps is closer to the valence band or to the conduction band. However, on the basis of reported DFT calculations on InAs QDs,[9,11] we ascribe them to surface states originating from undercoordinated As atoms residing between the valence band and midgap. The reason these surface states dominate the trap distribution in DFT calculations is that typical ligands used in the synthesis and processing of colloidal QDs bind stronger to surface cations, than to surface anions. Consequently, surface cations are assumed to be passivated (with, e.g., bromide, fluoride, oleate, or amines), while many surface As atoms remain undercoordinated.

After the *in situ* InF_3 treatment, the trap density is significantly reduced. The midgap trap density (integrated over trap energy) decreases from 1.7×10^{18} cm^{-3} to 3.3×10^{17} cm^{-3} (Figures 6G, H and S13). This shows that the InF_3 treatment is effective in removing dangling bonds on As sites by Z-type passivation, similar to what we found on InP QDs, where InF_3 passivated dangling bonds on undercoordinated P atoms.[23,25] Considering that the QDs we used in devices have a size of 6.5 nm, the extracted number of traps per QD is around 0.26 and 0.05 for the untreated and *in situ* InF_3-treated samples, respectively. However, we expect the trap density of the untreated InAs QDs to be larger than 1 since PLQY of QD dispersion is less than 1%. We ascribe this inconsistency to the error in the determination of V_{bi} and W in the two samples. In addition, it is conceivable that the TAS is not equally sensitive to all traps, and specifically detects traps states near the middle of the gap.

From the above temperature-dependent characteristics of InAs QDs-based SWIR photodetectors we conclude that deep trap states dominate the dark current, as evidenced by the dark current activation energy of $E_a \approx E_g/2$ and the large density of midgap trap states measured in with thermal admittance spectroscopy in the untreated device. The *in situ* InF_3 treatment significantly passivates surface trap states originating from undercoordinated As atoms, lowering the dark current density by an order of magnitude and thus improving the shot-noise limited specific detectivity. These results directly connect surface trap passivation with dark-current suppression in InAs QD photodetectors.

CONCLUSIONS

In summary, we have demonstrated that treatments with InF_3 significantly improve surface passivation of InAs QDs, yielding better optical and electronic performance: InF_3-treated InAs QDs exhibit enhanced PL and, when incorporated into devices, an order-of-magnitude reduction in the dark current density alongside a marked increase in the calculated specific detectivity assuming shot-noise-limited. Temperature-dependent dark current and thermal admittance spectroscopy measurements reveal that deep trap states dominate the electrical characteristics of InAs QD photodetectors. The *in situ* InF_3 treatment effectively suppresses these traps, leading to a reduced dark current and improved the device performance. However, achieving these improvements can introduce challenges, such as QD film roughening and reduced colloidal stability after fluorination. Moving forward, a layer-by-layer approach may help maximize surface passivation while preserving film morphology. In parallel, solution-processable inks are ideal for future device fabrication. Engineering surface ligands to retain sufficient surface charge or steric stabilization after fluoride addition could maintain the colloidal stability during solution-phase treatments. On the other hand, choosing more compatible solvents with the fluorinated QD surface may provide a route to achieve stable QD dispersions. These strategies promise to further optimize the device performance and stability, bringing efficient, low-cost, and RoHS-compliant InAs QD SWIR photodetectors.

EXPERIMENTAL SECTION

Materials

Indium(III) bromide ($InBr_3$, 99%), indium acetate (99.99%), ammonium acetate (AA, ≥97%), palmitic acid (≥99%), octylamine (99%), butylamine (≥99%), dry lithium perchlorate ($LiClO_4$, battery grade, 99.99% trace metal basis), anhydrous hexadecane (≥99%), anhydrous *N*,*N*-dimethylformamide (DMF, ≥99.8%), anhydrous *n*-hexane (97%), anhydrous *n*-octane (≥99%), anhydrous toluene (99.8%), anhydrous tetrachloroethylene (TCE, ≥99%), and anhydrous propylene carbonate (99.7%) were purchased from Sigma-Aldrich. Indium fluoride (InF_3, 99.95%) was purchased from Alfa Aesar. Benzoyl fluoride (BenF, ≥98.0%) and methylamine (ca. 2 M in DMF) were purchased from TCI Europe. Indium(III) chloride ($InCl_3$, >99.999%), tris(diethylamino)phosphine (97%), oleylamine (>96%, prim. amine, 80−90% C18 content), and anhydrous ethanol were purchased from Acros Organics. Trisdimethylaminoarsine (99%) and tri-*n*-octylphosphine (minimum 97%) were ordered from Strem Chemicals. Oleylamine was dried over CaH_2 and consequently vacuum distilled. Octylamine was degassed at 100 °C at 0.2 mbar for 5 h and stored in the glovebox for future use. Other chemicals were used as received. The InAs-OA QDs were purchased from Quantum Solutions.

Synthesis of In(As,P)-OlNH$_2$/Cl QDs

In a glovebox, 1.4 mL of distilled oleylamine, 100 mg of $InCl_3$, and a stir bar were placed in a 25 mL three-neck flask. The flask was then taken out of the glovebox and connected to a Schlenk line under inert gas. The mixture was degassed at 120 °C for 1 h. In another vessel, 370 μL of tris(diethylamino)phosphine was mixed with 1.5 mL of oleylamine, heated to 120 °C with stirring until the gas release stopped, and then cooled down to room temperature. After degassing, the reaction temperature was set to 270 °C. During the heating process, a mixture of 85 μL of trisdimethylaminoarsine and 500 μL of tri-*n*-octylphosphine was injected at 170 °C under nitrogen, and the transaminated aminophosphine reagent was injected into the reaction flask at 210 °C. After these injections, the temperature reached 270 °C and kept for 1 h. After cooling the reaction to 80 °C, anhydrous degassed toluene was added. The product was purified by repeated precipitation and redispersion using toluene as the solvent and ethanol as the nonsolvent. After the final redispersion in toluene, the QDs dispersion was filtered through a 0.45-μm-pore-size syringe filter.

Solution-Phase InF_3 Treatment

The procedure is adapted from the method previously reported by Stam et al.[23] In a typical InF_3 treatment in hexadecane, 50 mg of InF_3 and 18 mg of indium palmitate were added to 2 mg of In(As,P)-OlNH$_2$/Cl QDs or InAs-OA QDs in 0.5 mL of hexadecane in a glass vial. The vial was then heated to 180 °C and stirred for 60 min. After the treatment, 2.5 mL of anhydrous TCE was added to the vial and filtered for characterization. For InF_3 treatment in DMF, only 50 mg of InF_3 was added to 2 mg of ligand-exchanged InAs QDs in 0.5 mL of anhydrous DMF in a glass vial. The vial was then heated to 150 °C and stirred for 30 min. After the treatment, 2.5 mL of anhydrous DMF was added to the vial and filtered for characterization.

Ligand Exchange

In the glovebox, the solution-phase ligand exchange is based on the procedure reported by Sun et al.[15] A total of 0.18 g of $InBr_3$ and 0.023 g of AA were added to 5 mL of anhydrous DMF to make a ligand-exchange solution. A total of 5 mL of QDs dispersed in *n*-octane with a concentration of 10 mg mL^{-1} was added to the ligand exchange solution, then vortexed, and centrifuged to facilitate transfer into the

Downloaded from pubs.acs.org/ancac3/article-pdf/20/34/23822/6990153/acsnano.6c06196.pdf by TU DELFT user on 22 September 2026

https://doi.org/10.1021/acsnano.6c06196
ACS Nano 2026, 20, 23822−23836

DMF phase. This resulted in an octane phase with exchanged ligands and a DMF phase with QDs. The octane phase was removed, and fresh octane was added again to extract the exchanged ligands to further purify the QDs. This process was repeated three times. The QDs were subsequently precipitated with anhydrous toluene, redispersed in anhydrous DMF, and filtered for the optical characterization and device fabrication.

Solid-State *In Situ* InF_3 Treatment

In the glovebox, InAs QD films were spin-coated on quartz substrates ($2.54 \times 1 \times 0.11$ cm^3) using a 200 mg mL^{-1} DMF dispersion of ligand-exchanged QDs, followed by annealing at 150 °C for 10 min. BenF and primary amines (octylamine, butylamine, or methylamine) were dissolved in hexadecane to prepare 56 mM and 57 mM stock solutions, respectively. Treatment parameters were systematically varied: (1) amine chain length was altered using different amines at a fixed BenF amount (5 μmol) and BenF:amine ratio of 1:1.5; (2) BenF:amine molar ratio was adjusted by fixing BenF at 5 μmol while varying octylamine (7.5−10 μmol); (3) total BenF amount was tuned (2−50 μmol) while keeping the ratio constant at 1:1.5. The total volume of the treatment solution was fixed to be 3 mL by adding hexadecane according to the volume of amine and BenF solution. In a typical treatment, hexadecane and amine solution were added to a Petri dish and heated to 150 °C. InAs QD film on quartz substrate was immersed and then BenF solution was added dropwise within 30 s. After 15 min of treatment, the Petri dish was removed from hot plate and slowly cooled for 15 min to prevent film cracking due to fast cooling. The sample was rinsed three times with anhydrous hexane and dried at 50 °C for 10 min before characterization.

Optical Characterization

The absorption spectra were recorded by using a PerkinElmer Lambda 1050 UV/vis/NIR spectrophotometer. The PL spectra were obtained by using an Edinburgh Instruments FLS980 spectrofluorometer equipped with a 450 W xenon lamp. Absolute PLQYs were measured by using an Edinburgh Instruments FLS980 spectrofluorometer equipped with a calibrated integrating sphere. The excitation wavelengths for QD dispersions in TCE and QD films on quartz were 700 and 532 nm, respectively.

X-ray Photoelectron Spectroscopy

QD dispersions were drop-cast on conductive aluminum substrates inside a nitrogen-filled glovebox. The samples were vacuum transferred to the instrument. Measurements were performed on a Thermo Scientific K-Alpha equipped with Al Kα source. During the measurements, a flood gun was used to prevent charging of the samples. Spectra were corrected according to the main line of carbon 1S peak, set to be 284.8 eV.

Transmission Electron Microscopy

Samples were prepared by drop-casting QD dispersions onto the carbon-coated copper TEM grids. Images were obtained using a JEOL JEM1400Plus electron microscope operated at 120 kV. To obtain size distributions, TEM images were analyzed using NanoMetrics software developed by Pepijn Verscheure from Ghent University.

ζ-Potential Measurement

The measurements were conducted using a Zetasizer Nano ZS (Malvern Instruments, Inc.) with a dip cell equipped with palladium electrodes (ZEN1002, Malvern Instruments, Inc.) in a quartz cuvette. Each sample was measured three times, with each ζ-potential measurement comprising several scans of 100 runs under high-resolution mode.

Atomic Force Microscopy

Images were taken by using a Bruker Dimension Icon atomic force microscope. The ScanAsyst experiment mode was selected to image using SCANASYST-AIR-HIP tips.

Transient Absorption Spectroscopy

The measurements were performed using a Yb:KGW laser oscillator (Pharos SP, Light Conversion) generating 180 fs pulses at 1028 nm and 5 kHz repetition rate. The majority of the fundamental beam was directed through an optical parametric amplifier with a second harmonic module (Orpheus, Light Conversion) to generate pump pulses tunable between 310 and 1500 nm. A small portion of the 1028 nm beam was used to generate a broadband probe (480−1600 nm) via supercontinuum generation in a sapphire crystal. Pump and probe beams overlapped on the sample at an angle of ∼8°, with temporal delay (up to 3 ns) controlled by an automated delay stage. The pump beam was modulated at 2.5 kHz with a mechanical chopper. The probe beam, after transmission through the sample, was directed to a detector (Helios, Ultrafast Systems), while the pump beam was blocked. To minimize scattered pump light, orthogonal polarization was maintained between pump and probe beams. TA signals were calculated as $\Delta A = \log_{10}(I_{on}/I_{off})$, and probe chirp was corrected by polynomial fitting to the coherent artifact. The InAs QD films on quartz substrates were loaded into an airtight sample holder inside a nitrogen filled glovebox. Samples were excited at 700 nm in all measurements. The absorbed photons per QD, i.e., $\langle N_{abs}\rangle$, is determined by 1S absorption bleach (ΔA). For InAs QDs, the band-edge degeneracies of electron and hole are 2 and 4, respectively.[51] One exciton should block five absorption transitions and generate one stimulated emission. Therefore, $\langle N_{abs}\rangle$ is calculated by $4\Delta A/3A_0$.[67]

Microwave Conductivity Measurements

All microwave measurements are performed in an airtight resonance cavity measurement cell, which was loaded in the glovebox. DMC measurements were performed in the dark by sweeping the microwave frequency between 8.5 and 12.1 GHz. Meanwhile, the reflected microwave power is continuously measured to determine the absorbed power (ΔP). Usually, the DMC data is normalized ($\frac{\Delta P}{P}$), where P is the initial power (∼100 mW). The microwave frequencies that result in a standing wave in the cavity that is used as a measurement cell produce a dip in the frequency spectrum. The dip can be fitted to quantify the dark conductivity in the sample. Here, DMC data of the quartz substrate is used as a reference of the lower detection limit for measuring the background conductivity. The bare quartz dips are then compared to those of quartz with the QD film on top to obtain the dark conductivity of the film. Time-resolved microwave conductivity (TRMC) measurements are done using pulsed laser illumination (λ = 700 nm, 10 Hz repetition rate, 3−5 ns at fwhm) to study the photoconductivity of the films. The intensity of the laser is tuned by a set of neutral density filters. The generation and immobilization of carriers is reflected by a transient change in the microwave power ($\frac{\Delta P(t)}{P}$) and related to the change in photoconductivity [$\Delta G(t)$] using

$$\frac{\Delta P(t)}{P} = -K\Delta G(t) = -K\beta L\Delta\sigma(t)$$

where K is a predetermined sensitivity factor, β is a geometric factor that considers the inner dimensions of the cavity, and L is the sample thickness. Furthermore, a TRMC signal is typically reported normalized to reflect the sum of the electron and hole mobility ($\mu_e + \mu_h$) and the yield (Φ_{max}), which is defined as

$$\Phi_{max} = \frac{Ln}{F_A I_0}$$

Now using the fact that the conductivity (σ) scales with the number of free electrons and holes (n_e and n_h) and their respective mobilities ($\mu_e + \mu_h$), as described by

$$\sigma = e(\mu_e n_e + \mu_h n_h)$$

The yield mobility product can be written in the form

$$\varphi(\mu_e + \mu_h) = \frac{\Delta G}{\beta e F_A I_0}$$

Electrochemically Gated Transistor Measurements

The electrochemical cell consists of QD films spin coated on glass substrates with customized gold interdigitated electrodes (IDEs) as

Downloaded from pubs.acs.org/ancac3/article-pdf/20/34/23822/6990153/acsnano.6c06196.pdf by TU DELFT user on 22 September 2026

https://doi.org/10.1021/acsnano.6c06196
ACS Nano 2026, 20, 23822−23836

working electrodes (WEs), a silver pseudoreference electrode (RE), and a platinum sheet counter electrode (CE) immersed in a 0.1 M $LiClO_4$ propylene carbonate electrolyte solution. The width of the source−drain gap is 25 μm, and the total gap length is 6.8 cm. The measurement was performed by applying a gate potential on both source and drain electrodes until equilibrium was reached (~10 s). Afterward, a small cyclic source−drain bias sweep (±5 mV) was applied, and the current was measured at both source and drain electrodes. Absorption measurements were synchronized with source−drain bias sweeps, which accurately determines the charge carrier density by monitoring the 1S absorption bleaching.

The in-plane conductance G was determined by the slope of the $I-V$ curve. The in-plane conductivity σ was calculated as

$$\sigma = \frac{Gw}{lh}$$

where w is the source−drain gap width, l is the total gap length, and h is the height of the QD films.

The charge carrier density n is determined by

$$n = \frac{g\Delta A_{1S}}{A_{0,1S}}\frac{1}{2V_{QD}}$$

where g is the degeneracy of the 1S electron level ($g = 2$ for InAs QDs), $A_{0,1S}$ is the band edge absorbance at the open-circuit potential, and ΔA_{1S} is the differential absorbance as a function of the applied gate voltage. V_{QD} is the volume of a QD. We assume that the packing density in a QD film is 50%.

The in-plane mobility can be calculated as

$$\mu = \frac{\sigma}{ne}$$

where e is the elementary charge and n is the charge carrier density. The error bar in mobility is determined by the detection limit of SEC measurements which is ±1 mOD.

Device Fabrication

The photodiodes were fabricated on silicon substrates prepatterned with TiN electrodes. The cleaned substrates were transferred into a high-vacuum chamber (base pressure 10^{-7}−10^{-8} Torr) for the deposition of NiO_x films. The NiO_x films were subsequently annealed in air at 300 °C for 5 min. After cooling to room temperature, the substrates were transferred to a nitrogen-filled glovebox for QD layer deposition. QDs were spin-coated from the InBr/AA ligand-exchanged DMF ink with a concentration of 100 mg mL^{-1} on the substrates and annealed. For *in situ* InF_3 treatment on devices, stock solutions of BenF and octylamine in hexadecane with concentrations of 77 and 59 mM, respectively, were prepared. The substrates with QD layers were submerged in a beaker with 3.6 mL of hexadecane. A certain amount of an octylamine stock solution was added. The solution was heated to 150 °C, and BenF was then added dropwise within 30 s with an amount to keep the molar ratio of BenF:octylamine constant (1:1.5). The amount of precursors were optimized to passivate surface traps while maintaining morphology. The optimal volumes of octylamine and BenF stock solutions used for devices in Figures 5 and 6 were 538 and 279 μL, respectively. The solution was kept at 150 °C for 15 min, followed by removal of the heat source and allowing it to cool at room temperature for 15 min. The sample was then rinsed with hexane and dried at 70 °C for 10 min. Subsequently, TiO_x layer was deposited on both the untreated and *in situ* InF_3-treated devices. Finally, the devices were completed by sputtering an ITO top contact.

Device Characterization

The dark $j-V$ characteristics were measured by using a Keithley 2612B precision sourcemeter. The voltage was swept from +5 to −5 V with a step size of 0.01 V and a delay time of 0.01 s between steps. The photocurrent measurements were performed by using a Paios System (Fluxim AG, Switzerland). The devices were illuminated with a 1200 nm LED at a maximum irradiance of 3.5 mW cm^{-2}. The voltage was swept from +5 to −5 V with a step size of 0.1 V and a delay time of 0.1 s between steps.

The EQE measurements were performed using a Stanford SR830 lock-in amplifier coupled with a monochromator and a 145 W halogen lamp. The signal was amplified by a Stanford Research System SR570 low-noise current preamplifier. Calibration was done using a calibrated Ge photodiode. The shot-noise-limited specific detectivity, D^*_{shot}, was calculated as

$$D^*_{shot} = \mathrm{EQE} \times \frac{\lambda}{hc}\sqrt{\frac{e}{2J_d}}$$

where EQE is the external quantum efficiency, λ is the incident light wavelength, h is Planck's constant, c is the speed of light, e is the elementary charge, and J_d is the dark current.

The temperature-dependent dark $j-V$ and thermal admittance spectroscopy measurements were performed using the Paios system (Fluxim AG, Switzerland), coupled to a VPF-100 Series cryostat from Lake Shore Cryotronics. The dark $j-V$ was measured using a voltage sweep from +5 to −5 V, a step size of 0.1 V, and a delay time of 0.1 s. The impedance spectroscopy was measured in a frequency range from 10 MHz to 5 Hz and sampled at 51 logarithmically spaced frequency points. The measurements were conducted at a DC bias of 0 V with an AC modulation amplitude of 35 mV.

$C-V$ measurements were also carried out with the custom Paios system at 300 K. The measurements used a 35 mV AC modulation at a frequency of 1 kHz. During the measurement, the DC voltage offset was swept from +5 to −5 V.

The SEM cross-sectional images of the InAs QD photodetectors before and after *in situ* InF_3 treatment were obtained using an FEI Nova 200 equipped with an in-lens detector. Before imaging, a thin layer of platinum was deposited on the cross section to enhance conductivity.

■ ASSOCIATED CONTENT

Supporting Information

The Supporting Information is available free of charge at https://pubs.acs.org/doi/10.1021/acsnano.6c06196.

TEM images of InAs QDs and XPS data of InAs QDs before and after InF_3 treatment in nonpolar solvent, PL spectra of direct InF_3- and *in situ* InF_3-treated InAs-Br/AA QD films, fluence-dependent TA decays and TRMC traces, summary of dark conductivities and dark carrier densities based on TRMC and DMC measurements, overview of electrochemically gated transistor measurements, SEM cross-sectional images of the devices before and after *in situ* InF_3 treatment, additional dark $j-V$ characteristics of individual devices on one substrate, Arrhenius plots obtained from temperature-dependent $j-V$ measurements, Supplementary Note 1 about the theoretical background and data processing procedure of thermal admittance spectroscopy measurements, $\omega dc/d\omega$ vs ω plot, Arrhenius plot of $C-f$ spectra measured from 285 to 330 K of the untreated device, and comparison of the trap density distribution before and after treatment (PDF)

■ AUTHOR INFORMATION

Corresponding Author

Arjan J. Houtepen − *Optoelectronic Materials Section, Faculty of Applied Sciences, Delft University of Technology, 2629 HZ Delft, The Netherlands;* orcid.org/0000-0001-8328-443X; Email: a.j.houtepen@tudelft.nl

Authors

Hua Chen − *Optoelectronic Materials Section, Faculty of Applied Sciences, Delft University of Technology, 2629 HZ Delft, The Netherlands;* orcid.org/0009-0002-3391-9403

Downloaded from pubs.acs.org/ancac3/article-pdf/20/34/23822/6690153/acsnano.6c06196.pdf by TU DELFT user on 22 September 2026

https://doi.org/10.1021/acsnano.6c06196
ACS Nano 2026, 20, 23822−23836

Boris B. Claus − *Optoelectronic Materials Section, Faculty of Applied Sciences, Delft University of Technology, 2629 HZ Delft, The Netherlands; IMEC, 3001 Leuven, Belgium*
Wenya Song − *IMEC, 3001 Leuven, Belgium;* orcid.org/0000-0003-1988-9324
Marina Vildanova − *IMEC, 3001 Leuven, Belgium*
Lara M. van der Poll − *Optoelectronic Materials Section, Faculty of Applied Sciences, Delft University of Technology, 2629 HZ Delft, The Netherlands*
Anne van Aken − *Optoelectronic Materials Section, Faculty of Applied Sciences, Delft University of Technology, 2629 HZ Delft, The Netherlands*
Yan B. Vogel − *Optoelectronic Materials Section, Faculty of Applied Sciences, Delft University of Technology, 2629 HZ Delft, The Netherlands;* orcid.org/0000-0003-1975-7292
Jing Bai − *Physics and Chemistry of Nanostructures, Department of Chemistry, Ghent University, 9000 Gent, Belgium; Center for Nano and Biophotonics, Ghent University, 9000 Gent, Belgium;* orcid.org/0000-0002-3361-0433
Yun Hai − *Zernike Institute for Advanced Materials, University of Groningen, Groningen 9747AG, The Netherlands;* orcid.org/0009-0008-8303-9870
Yigithan M. Kose − *IMEC, 3001 Leuven, Belgium; Department of Electrical Engineering (ESAT), KU Leuven, 3001 Leuven, Belgium*
Maria Isabel Pintor Monroy − *IMEC, 3001 Leuven, Belgium;* orcid.org/0000-0003-0403-602X
Loredana Protesescu − *Zernike Institute for Advanced Materials, University of Groningen, Groningen 9747AG, The Netherlands;* orcid.org/0000-0002-9776-9881
Tom J. Savenije − *Optoelectronic Materials Section, Faculty of Applied Sciences, Delft University of Technology, 2629 HZ Delft, The Netherlands;* orcid.org/0000-0003-1435-9885
Zeger Hens − *Physics and Chemistry of Nanostructures, Department of Chemistry, Ghent University, 9000 Gent, Belgium; Center for Nano and Biophotonics, Ghent University, 9000 Gent, Belgium;* orcid.org/0000-0002-7041-3375
Itai Lieberman − *IMEC, 3001 Leuven, Belgium;* orcid.org/0000-0002-5188-6652

Complete contact information is available at: https://pubs.acs.org/10.1021/acsnano.6c06196

Author Contributions

The manuscript was written through contributions of all authors. All authors have given approval to the final version of the manuscript.

Funding

This publication is part of the project Quantum Dots for Advanced Lighting Applications (QUALITy) with Project 17188 of the Open Technology Programme, which is (partly) financed by the Dutch Research Council (NWO). H.C. and Y.H. thank the China Scholarship Council for funding (File Nos. 202206120047 and 202106150016).

Notes

The authors declare no competing financial interest.

■ ACKNOWLEDGMENTS

The authors thank Xiaohui Liu and Bart Boshuizen for assistance with XPS measurements and Bahiya Ibrahim, Jos Thieme, and Pierre Retief for technical assistance with TA and electrochemically gated transistor measurements. The authors also thank Hong Hai Nguyen for assistance with the temperature-dependent dark $j-V$ and thermal admittance spectroscopy measurements.

■ REFERENCES

(1) Zhang, Y.; Chen, J.; Yang, J.; Fu, M.; Cao, Y.; Dong, M.; Yu, J.; Dong, S.; Yang, X.; Shao, L.; Hu, Z.; Cai, H.; Liu, C.; Huang, F. Sensitive SWIR Organic Photodetectors with Spectral Response Reaching 1.5 μm. *Adv. Mater.* **2024**, *36* (41), 2406950.
(2) Leemans, J.; Pejović, V.; Georgitzikis, E.; Minjauw, M.; Siddik, A. B.; Deng, Y.; Kuang, Y.; Roelkens, G.; Detavernier, C.; Lieberman, I.; Malinowski, P. E.; Cheyns, D.; Hens, Z. Colloidal III−V Quantum Dot Photodiodes for Short-Wave Infrared Photodetection. *Adv. Sci.* **2022**, *9* (17), 2200844.
(3) Pejović, V.; Georgitzikis, E.; Lieberman, I.; Malinowski, P. E.; Heremans, P.; Cheyns, D. Photodetectors Based on Lead Sulfide Quantum Dot and Organic Absorbers for Multispectral Sensing in the Visible to Short-Wave Infrared Range. *Adv. Funct. Mater.* **2022**, *32* (28), 2201424.
(4) Pejovic, V.; Georgitzikis, E.; Lee, J.; Lieberman, I.; Cheyns, D.; Heremans, P.; Malinowski, P. E. Infrared Colloidal Quantum Dot Image Sensors. *IEEE Trans. Electron Devices* **2022**, *69* (6), 2840−2850.
(5) Tang, X.; Ackerman, M. M.; Chen, M.; Guyot-Sionnest, P. Dual-Band Infrared Imaging Using Stacked Colloidal Quantum Dot Photodiodes. *Nat. Photonics* **2019**, *13* (4), 277−282.
(6) Deng, Y.; Pang, C.; Kheradmand, E.; Leemans, J.; Bai, J.; Minjauw, M.; Liu, J.; Molkens, K.; Beeckman, J.; Detavernier, C.; Geiregat, P.; Van Thourhout, D.; Hens, Z. Short-Wave Infrared Colloidal QD Photodetector with Nanosecond Response Times Enabled by Ultrathin Absorber Layers. *Adv. Mater.* **2024**, *36* (28), 2402002.
(7) Bahmani Jalali, H.; De Trizio, L.; Manna, L.; Di Stasio, F. Indium Arsenide Quantum Dots: An Alternative to Lead-Based Infrared Emitting Nanomaterials. *Chem. Soc. Rev.* **2022**, *51* (24), 9861−9881.
(8) Zhu, D.; Bellato, F.; Bahmani Jalali, H.; Di Stasio, F.; Prato, M.; Ivanov, Y. P.; Divitini, G.; Infante, I.; De Trizio, L.; Manna, L. $ZnCl_2$ Mediated Synthesis of InAs Nanocrystals with Aminoarsine. *J. Am. Chem. Soc.* **2022**, *144* (23), 10515−10523.
(9) Hens, Z.; Llusar, J.; Infante, I. Fuzzy Band Structure of Quantum Dots by Bloch Orbital Expansion: Unconventional Insights into Geometric-Electronic Structure Relations. *ACS Nano* **2025**, *19* (8), 8227−8237.
(10) Zhu, D.; Llusar, J.; Asaithambi, A.; Liu, Z.; Bes, R.; Prieur, D.; Karakkal, H. H.; Prato, M.; Brovelli, S.; Saleh, G.; Panda, S.; Infante, I.; De Trizio, L.; Manna, L. Unveiling the Role of $ZnCl_2$ in Enhancing the Photoluminescence Efficiency of Amino-As-Based InAs@ZnSe Quantum Dots. *ACS Nano* **2025**, *19* (39), 34807−34818.
(11) De Vlamynck, N.; Llusar, J.; Infante, I.; Hens, Z. Surface Orbitals and Facet Tolerance in III-V Quantum Dots*ACS Nano* **2026**, *20*, 21984−21996. .
(12) Panda, S.; Zhu, D.; Goldoni, L.; Asaithambi, A.; Brescia, R.; Saleh, G.; De Trizio, L.; Manna, L. Overcoming the Short-Wave Infrared Barrier in the Photoluminescence of Amino-As-Based InAs Quantum Dots. *Adv. Opt. Mater.* **2025**, *13* (29), e01512.
(13) Kim, S.; Yeon, S.; Lee, M.; Jin, J.; Shin, S.; Gwak, N.; Jeong, I.; Jang, H.; Hwang, G. W.; Oh, N. Chemically and Electronically Active Metal Ions on InAs Quantum Dots for Infrared Detectors. *NPG Asia Mater.* **2023**, *15* (1), 30.
(14) Song, J. H.; Choi, H.; Pham, H. T.; Jeong, S. Energy Level Tuned Indium Arsenide Colloidal Quantum Dot Films for Efficient Photovoltaics. *Nat. Commun.* **2018**, *9* (1), 4267.
(15) Sun, B.; Najarian, A. M.; Sagar, L. K.; Biondi, M.; Choi, M.; Li, X.; Levina, L.; Baek, S.; Zheng, C.; Lee, S.; Kirmani, A. R.; Sabatini, R.; Abed, J.; Liu, M.; Vafaie, M.; Li, P.; Richter, L. J.; Voznyy, O.; Chekini, M.; Lu, Z.; García de Arquer, F. P.; Sargent, E. H. Fast Near-Infrared Photodetection Using III−V Colloidal Quantum Dots. *Adv. Mater.* **2022**, *34* (33), 2203039.
(16) Jung, B. K.; Yoo, H.; Seo, B.; Choi, H. J.; Choi, Y. K.; Kim, T. H.; Oh, N.; Kim, S. Y.; Kim, S.; Lee, Y.; Shim, J. W.; Park, H. Y.; Hwang, G.

Downloaded from pubs.acs.org/ancac3/article-pdf/20/34/23822/6690153/acsnano.6c06196.pdf by TU DELFT user on 22 September 2026

W.; Ng, T. N.; Oh, S. J. High-Affinity Ligand-Enhanced Passivation of Group III−V Colloidal Quantum Dots for Sensitive Near-Infrared Photodetection. *ACS Energy Lett.* **2024**, *9* (2), 504−512.
(17) Si, M.; Jee, S.; Yang, M.; Kim, D.; Ahn, Y.; Lee, S.; Kim, C.; Bae, I.; Baek, S. Colloidal InAs Quantum Dot-Based Infrared Optoelectronics Enabled by Universal Dual-Ligand Passivation. *Adv. Sci.* **2024**, *11* (13), 2306798.
(18) Xia, P.; Sun, B.; Biondi, M.; Xu, J.; Atan, O.; Imran, M.; Hassan, Y.; Liu, Y.; Pina, J. M.; Najarian, A. M.; Grater, L.; Bertens, K.; Sagar, L. K.; Anwar, H.; Choi, M.; Zhang, Y.; Hasham, M.; García de Arquer, F. P.; Hoogland, S.; Wilson, M. W. B.; Sargent, E. H. Sequential Co-Passivation in InAs Colloidal Quantum Dot Solids Enables Efficient Near-Infrared Photodetectors. *Adv. Mater.* **2023**, *35* (28), 2301842.
(19) Xia, P.; Wang, S.; Chen, Y.; Gulsaran, A.; Zhang, Y.; Vafaie, M.; Imran, M.; Najarian, A. M.; Liu, Y.; Ban, H.; Sagar, L. K.; Yavuz, M.; Sargent, E. H. Improved Facet and Edge Passivation in Near-Infrared III-V Colloidal Quantum Dot Photodetectors. *Adv. Mater.* **2025**, *37* (18), 2419020 .
(20) Siddik, A. B.; Song, W.; Georgitzikis, E.; Vildanova, M.; Jin, M.; Berghmans, F.; Lieberman, I.; Malinowski, P. E.; Conard, T.; Cheyns, D.; Heremans, P. InAs Colloidal Quantum Dot Photodiode Stack for CMOS-Integrated Infrared Imaging. *ACS Nano* **2025**, *19* (36), 32780−32787.
(21) Liu, J.; Liu, P.; Shi, T.; Ke, M.; Xiong, K.; Liu, Y.; Chen, L.; Zhang, L.; Liang, X.; Li, H.; Lu, S.; Lan, X.; Niu, G.; Zhang, J.; Fei, P.; Gao, L.; Tang, J. Flexible and Broadband Colloidal Quantum Dots Photodiode Array for Pixel-Level X-Ray to near-Infrared Image Fusion. *Nat. Commun.* **2023**, *14* (1), 5352.
(22) Zherebetskyy, D.; Zhang, Y.; Salmeron, M.; Wang, L.-W. Tolerance of Intrinsic Defects in PbS Quantum Dots. *J. Phys. Chem. Lett.* **2015**, *6* (23), 4711−4716.
(23) Stam, M.; Almeida, G.; Ubbink, R. F.; van der Poll, L. M.; Vogel, Y. B.; Chen, H.; Giordano, L.; Schiettecatte, P.; Hens, Z.; Houtepen, A. J. Near-Unity Photoluminescence Quantum Yield of Core-Only InP Quantum Dots via a Simple Postsynthetic InF_3 Treatment. *ACS Nano* **2024**, *18* (22), 14685−14695.
(24) Kim, T.-G.; Zherebetskyy, D.; Bekenstein, Y.; Oh, M. H.; Wang, L.-W.; Jang, E.; Alivisatos, A. P. Trap Passivation in Indium-Based Quantum Dots through Surface Fluorination: Mechanism and Applications. *ACS Nano* **2018**, *12* (11), 11529−11540.
(25) Ubbink, R. F.; Almeida, G.; Iziyi, H.; du Fossé, I.; Verkleij, R.; Ganapathy, S.; van Eck, E. R. H.; Houtepen, A. J. A Water-Free In Situ HF Treatment for Ultrabright InP Quantum Dots. *Chem. Mater.* **2022**, *34* (22), 10093−10103.
(26) Valleix, R.; Zhang, W.; Jordan, A. J.; Guillemeney, L.; Castro, L. G.; Zekarias, B. L.; Park, S. V.; Wang, O.; Owen, J. S. Metal Fluorides Passivate II−VI and III−V Quantum Dots. *Nano Lett.* **2024**, *24* (19), 5722−5728.
(27) Leemans, J.; Respekta, D.; Bai, J.; Braeuer, S.; Vanhaecke, F.; Hens, Z. Formation of Colloidal In(As,P) Quantum Dots Active in the Short-Wave Infrared, Promoting Growth through Temperature Ramps. *ACS Nano* **2023**, *17* (20), 20002−20012.
(28) Srivastava, V.; Dunietz, E.; Kamysbayev, V.; Anderson, J. S.; Talapin, D. V. Monodisperse InAs Quantum Dots from Aminoarsine Precursors: Understanding the Role of Reducing Agent. *Chem. Mater.* **2018**, *30* (11), 3623−3627.
(29) Ginterseder, M.; Franke, D.; Perkinson, C. F.; Wang, L.; Hansen, E. C.; Bawendi, M. G. Scalable Synthesis of InAs Quantum Dots Mediated through Indium Redox Chemistry. *J. Am. Chem. Soc.* **2020**, *142* (9), 4088−4092.
(30) Grigel, V.; Dupont, D.; De Nolf, K.; Hens, Z.; Tessier, M. D. InAs Colloidal Quantum Dots Synthesis via Aminopnictogen Precursor Chemistry. *J. Am. Chem. Soc.* **2016**, *138* (41), 13485−13488.
(31) Joo, C.; Yeon, S.; Llusar, J.; Gul, S.; Park, C.; Lee, J.; Ha, J.; Jang, J.; Kwak, I. H.; Yun, H. J.; Kim, S. K.; Cho, Y.-H.; Infante, I.; Cho, H. Overcoming the Luminescence Efficiency Limitations of InP Magic-Sized Clusters. *J. Am. Chem. Soc.* **2025**, *147* (52), 48046−48059.
(32) Hu, C.; Channa, A. I.; Xia, L.; Li, X.; Li, Z.; Wang, Z. M.; Tong, X. Colloidal InAs Quantum Dots: Synthesis, Properties, and Optoelectronic Devices. *Adv. Funct. Mater.* **2025**, *35* (32), 2500280 .
(33) Kamath, A.; Guyot-Sionnest, P. The "Energy Gap Law" for Mid-Infrared Nanocrystals. *J. Chem. Phys.* **2024**, *160* (20), 200901 .
(34) Hines, M. A.; Scholes, G. D. Colloidal PbS Nanocrystals with Size-Tunable Near-Infrared Emission: Observation of Post-Synthesis Self-Narrowing of the Particle Size Distribution. *Adv. Mater.* **2003**, *15* (21), 1844−1849.
(35) Wehrenberg, B. L.; Wang, C.; Guyot-Sionnest, P. Interband and Intraband Optical Studies of PbSe Colloidal Quantum Dots. *J. Phys. Chem. B* **2002**, *106* (41), 10634−10640.
(36) Houtepen, A. J.; Sargent, E. H.; Infante, I.; Owen, J. S.; Green, P. B.; Schaller, R. D.; Bals, S.; Zeiske, S.; Stöferle, T.; Hens, Z. Colloidal Quantum Dots for Optoelectronics. *Nature Reviews Methods Primers* **2025**, *5* (1), 42.
(37) Dong, A.; Ye, X.; Chen, J.; Kang, Y.; Gordon, T.; Kikkawa, J. M.; Murray, C. B. A Generalized Ligand-Exchange Strategy Enabling Sequential Surface Functionalization of Colloidal Nanocrystals. *J. Am. Chem. Soc.* **2011**, *133* (4), 998−1006.
(38) Boles, M. A.; Ling, D.; Hyeon, T.; Talapin, D. V. The Surface Science of Nanocrystals. *Nat. Mater.* **2016**, *15* (2), 141−153.
(39) Hai, Y.; Gahlot, K.; Tanchev, M.; Mutalik, S.; Tekelenburg, E. K.; Hong, J.; Ahmadi, M.; Piveteau, L.; Loi, M. A.; Protesescu, L. Metal−Solvent Complex Formation at the Surface of InP Colloidal Quantum Dots. *J. Am. Chem. Soc.* **2024**, *146* (18), 12808−12818.
(40) Gao, Y.; Sandeep, C. S. S.; Schins, J. M.; Houtepen, A. J.; Siebbeles, L. D. A. Disorder Strongly Enhances Auger Recombination in Conductive Quantum-Dot Solids. *Nat. Commun.* **2013**, *4* (1), 2329.
(41) Gao, Y.; Talgorn, E.; Aerts, M.; Trinh, M. T.; Schins, J. M.; Houtepen, A. J.; Siebbeles, L. D. A. Enhanced Hot-Carrier Cooling and Ultrafast Spectral Diffusion in Strongly Coupled PbSe Quantum-Dot Solids. *Nano Lett.* **2011**, *11* (12), 5471−5476.
(42) Gilmore, R. H.; Lee, E. M. Y.; Weidman, M. C.; Willard, A. P.; Tisdale, W. A. Charge Carrier Hopping Dynamics in Homogeneously Broadened PbS Quantum Dot Solids. *Nano Lett.* **2017**, *17* (2), 893−901.
(43) van der Poll, L. M.; van Silfhout, N.; Nespoli, J.; van der Meer, M.; Boekhoff, R. K.; Bannenberg, L. J.; Smets, A. H. M.; Savenije, T. J. Additive-Free Sequential Thermal Evaporation of Near-Intrinsic Pb-Sn Perovskites. *Small Methods* **2025**, *9* (4), 2401246 .
(44) Nespoli, J.; van der Meer, M. J.; Heester, S.; Koning, J. S.; Boshuizen, B.; Koster, L. J. A.; Savenije, T. J. Quantitative Analysis of the Doping and Defect Density in Mixed Sn−Pb Perovskites Mediated by SnF_2. *Chem. Mater.* **2025**, *37* (19), 7611−7621.
(45) Talgorn, E.; Gao, Y.; Aerts, M.; Kunneman, L. T.; Schins, J. M.; Savenije, T. J.; van Huis, M. A.; van der Zant, H. S. J.; Houtepen, A. J.; Siebbeles, L. D. A. Unity Quantum Yield of Photogenerated Charges and Band-like Transport in Quantum-Dot Solids. *Nat. Nanotechnol.* **2011**, *6* (11), 733−739.
(46) Sandeep, C. S. S.; ten Cate, S.; Schins, J. M.; Savenije, T. J.; Liu, Y.; Law, M.; Kinge, S.; Houtepen, A. J.; Siebbeles, L. D. A. High Charge-Carrier Mobility Enables Exploitation of Carrier Multiplication in Quantum-Dot Films. *Nat. Commun.* **2013**, *4* (1), 2360.
(47) Yu, D.; Wang, C.; Guyot-Sionnest, P. *n*-Type Conducting CdSe Nanocrystal Solids. *Science* **2003**, *300* (5623), 1277−1280.
(48) Vanmaekelbergh, D.; Houtepen, A. J.; Kelly, J. J. Electrochemical Gating: A Method to Tune and Monitor the (Opto)Electronic Properties of Functional Materials. *Electrochim. Acta* **2007**, *53* (3), 1140−1149.
(49) Gudjonsdottir, S.; van der Stam, W.; Kirkwood, N.; Evers, W. H.; Houtepen, A. J. The Role of Dopant Ions on Charge Injection and Transport in Electrochemically Doped Quantum Dot Films. *J. Am. Chem. Soc.* **2018**, *140* (21), 6582−6590.
(50) Vogel, Y. B.; Stam, M.; Mulder, J. T.; Houtepen, A. J. Long-Range Charge Transport via Redox Ligands in Quantum Dot Assemblies. *ACS Nano* **2022**, *16* (12), 21216−21224.
(51) Vogel, Y. B.; Tao, R.; Chen, H.; Ferraresi, L. J. A.; Boehme, S. C.; Dirin, D. N.; Shorubalko, I.; Houtepen, A. J.; Kovalenko, M. V.

Downloaded from pubs.acs.org/ancac3/article-pdf/20/34/23822/6990153/acsnano.6c06196.pdf by TU DELFT user on 22 September 2026

Electrochemical Control over Electron Density of InAs Quantum Dots. *J. Am. Chem. Soc.* **2026**, *148*, 3938.
(52) Houtepen, A. J.; Vanmaekelbergh, D. Orbital Occupation in Electron-Charged CdSe Quantum-Dot Solids. *J. Phys. Chem. B* **2005**, *109* (42), 19634−19642.
(53) Chandler, R. E.; Houtepen, A. J.; Nelson, J.; Vanmaekelbergh, D. Electron Transport in Quantum Dot Solids: Monte Carlo Simulations of the Effects of Shell Filling, Coulomb Repulsions, and Site Disorder. *Phys. Rev. B* **2007**, *75* (8), No. 085325.
(54) Saha, S. K.; Guyot-Sionnest, P. Mid-Infrared Intraband Transitions in InAs Colloidal Quantum Dots. *ACS Nano* **2026**, *20* (6), 5199.
(55) Shockley, W.; Read, W. T. Statistics of the Recombinations of Holes and Electrons. *Phys. Rev.* **1952**, *87* (5), 835−842.
(56) Hall, R. N. Electron-Hole Recombination in Germanium. *Phys. Rev.* **1952**, *87* (2), 387−387.
(57) Kublitski, J.; Hofacker, A.; Boroujeni, B. K.; Benduhn, J.; Nikolis, V. C.; Kaiser, C.; Spoltore, D.; Kleemann, H.; Fischer, A.; Ellinger, F.; Vandewal, K.; Leo, K. Reverse Dark Current in Organic Photodetectors and the Major Role of Traps as Source of Noise. *Nat. Commun.* **2021**, *12* (1), 551.
(58) Ma, X.; Janssen, R. A. J.; Gelinck, G. H. Trap-Assisted Charge Generation and Recombination in State-of-the-Art Organic Photodetectors. *Adv. Mater. Technol.* **2023**, *8* (16), 2300234 .
(59) Wang, Z. P.; Gong, H. H.; Yu, X. X.; Hu, T. C.; Ji, X. L.; Ren, F.-F.; Gu, S. L.; Zheng, Y. D.; Zhang, R.; Ye, J. D. Traps Inhomogeneity Induced Conversion of Shockley−Read−Hall Recombination in NiO/β-Ga_2O_3 P^+−n Heterojunction Diodes. *Appl. Phys. Lett.* **2023**, *122* (15), 152102.
(60) Siddik, A. B.; Georgitzikis, E.; Hermans, Y.; Kang, J.; Kim, J. H.; Pejovic, V.; Lieberman, I.; Malinowski, P. E.; Kadashchuk, A.; Genoe, J.; Conard, T.; Cheyns, D.; Heremans, P. Interface-Engineered Organic Near-Infrared Photodetector for Imaging Applications. *ACS Appl. Mater. Interfaces* **2023**, *15* (25), 30534−30542.
(61) Wang, S.; Kaienburg, P.; Klingebiel, B.; Schillings, D.; Kirchartz, T. Understanding Thermal Admittance Spectroscopy in Low-Mobility Semiconductors. *J. Phys. Chem. C* **2018**, *122* (18), 9795−9803.
(62) Walter, T.; Herberholz, R.; Müller, C.; Schock, H. W. Determination of Defect Distributions from Admittance Measurements and Application to Cu(In,Ga)Se_2 Based Heterojunctions. *J. Appl. Phys.* **1996**, *80* (8), 4411−4420.
(63) Ip, A. H.; Thon, S. M.; Hoogland, S.; Voznyy, O.; Zhitomirsky, D.; Debnath, R.; Levina, L.; Rollny, L. R.; Carey, G. H.; Fischer, A.; Kemp, K. W.; Kramer, I. J.; Ning, Z.; Labelle, A. J.; Chou, K. W.; Amassian, A.; Sargent, E. H. Hybrid Passivated Colloidal Quantum Dot Solids. *Nat. Nanotechnol.* **2012**, *7* (9), 577−582.
(64) Bozyigit, D.; Volk, S.; Yarema, O.; Wood, V. Quantification of Deep Traps in Nanocrystal Solids, Their Electronic Properties, and Their Influence on Device Behavior. *Nano Lett.* **2013**, *13* (11), 5284−5288.
(65) Bothra, U.; Albaladejo-Siguan, M.; Vaynzof, Y.; Kabra, D. Impact of Ligands on the Performance of PbS Quantum Dot Visible−Near-Infrared Photodetectors. *Adv. Opt. Mater.* **2023**, *11* (1), 2201897 .
(66) Carr, J. A.; Elshobaki, M.; Chaudhary, S. Deep Defects and the Attempt to Escape Frequency in Organic Photovoltaic Materials. *Appl. Phys. Lett.* **2015**, *107* (20), 203302 .
(67) Grimaldi, G.; Geuchies, J. J.; van der Stam, W.; du Fossé, I.; Brynjarsson, B.; Kirkwood, N.; Kinge, S.; Siebbeles, L. D. A.; Houtepen, A. J. Spectroscopic Evidence for the Contribution of Holes to the Bleach of Cd-Chalcogenide Quantum Dots. *Nano Lett.* **2019**, *19* (5), 3002−3010.

Downloaded from pubs.acs.org/ancac3/article-pdf/20/34/23822/6990153/acsnano.6c06196.pdf by TU DELFT user on 22 September 2026

https://doi.org/10.1021/acsnano.6c06196
ACS Nano 2026, 20, 23822−23836